Modeling Clam-inspired Burrowing in Dry Sand using Cavity Expansion Theory and DEM

Sichuan Huang¹ and Junliang Tao^{2*}

¹Research Assistant, Center for Biomediated and Bioinspired Geotechnics, School of Sustainable Engineering and the Built Environment, Arizona State University, Tempe, AZ 85281.
²Associate Professor, Center for Biomediated and Bioinspired Geotechnics, School of Sustainable Engineering and the Built Environment, Arizona State University, Tempe, AZ 85281.
*Corresponding author; Email: jtao25@asu.edu

ABSTRACT

The Atlantic razor clam exhibits exceptional penetration performance in wet sands by periodically expanding and contracting its shell and foot during burrowing. Essentially, this periodic penetration movement can be simplified as a cyclic alternation of cylinder expansion and cone penetration, which are analogous to the geotechnical pressuremeter test and the cone penetration test. The dynamic penetration movement of the razor clam was simplified as four major connective steps—cylinder expansion, cone penetration, cylinder contraction and cylinder retraction—and the kinematics was parameterized based on the biological data. Using a simplified and idealized synthetic dry sand sample, we attempted to model the clam-inspired penetration process using two common geomechanics tools: an analytical model based on cavity expansion theory and a numerical discrete element method (DEM), and to showcase the advantages and limitations of these two approaches in the dynamic penetration modeling. In the analytical model, the four consecutive steps were assumed to be independent. The penetration resistance and energy consumption for each step were therefore roughly estimated using cavity expansion theory; in parallel, the independent cylinder expansion and cone penetration process as well as the claminspired coupled dynamic penetration process were also modeled using the DEM method. When the results were compared, it was found that the adopted cavity expansion theory solutions can predict the independent cylinder expansion and cone penetration behaviors, given that the parameters were carefully chosen and calibrated. However, it cannot capture the interference effect in a coupled dynamic penetration process. Specifically, the analytical model overestimates the cone penetration resistance of the coupled dynamic penetration process; the cylindrical shaft expansion causes stress release around the cone, leading to a reduction of the tip resistance as the cone continues to penetrate. The analytical model also underestimates the expansion pressure in the dynamic penetration process, which is attributed to the change in stress and fabric state caused by the cyclic expansion/contraction movement. Moreover, the clam-inspired dynamic penetration was found to reduce the energetic cost on the penetration of cone and shaft for about 36% and still maintain a slightly lower energy consumption with additional cost on the cyclic shaft expansion, compared with the pure cone penetration strategy. With a better future understanding of the highly effective and efficient self-burrowing behavior of natural burrowers, it is envisioned to develop self-burrowing robots for a spectrum of geotechnical applications.

Keywords: Razor clam, Dynamic penetration, Cavity expansion theory, DEM, Resistance, Energy

INTRODUCTION

A great many living organisms in nature inhabit an underground, particulate environment and have evolved unique and efficient ways to locomote though the substrate. For example, a reptile known as the common sandfish (*Scincus scincus*) undulates its body to effectively swim through a sandy substrate (Maladen et al. 2011); earthworms cyclically break the soil ahead of them to move through a cohesive substrate (Dorgan 2015); and nematodes move through a substrate via reciprocating motions (Wallace 1968). Similar subsurface traveling/penetration behavior is also ubiquitous in the plant kingdom: most natural roots penetrate through soils by alternating their growth in the radial and longitudinal directions (Abdalla et al. 1969), and many seeds bury themselves in the ground using awns, which change shape in response to the level of humidity in the environment and effectively drill the seed into the soil (Elbaum et al. 2007).

Among the natural burrowers, the Atlantic razor clam (Ensis directus) has been reported to have exceptional burrowing abilities that rely on a very simple body structure and control strategy (Trueman 1967). The body structure of the razor clam is composed of a slender rigid shell, two convex shell valves (which the clam rotates relative to each other through the use of a single degree-of-freedom elastic hinge ligament), and a dexterous tubular foot located at the bottom of the valves. The unique burrowing strategy used by razor clams has been described as a two-anchor system (Trueman 1967), which in general is a series of cyclic alterations of foot motion and valve motion. As shown in Fig. 1a, the coordination of foot and valves in a typical burrowing cycle can be divided into four consecutive stages: 1) the clam relaxes the hinge muscles, and the valves open and brace against the sand, serving as a penetration anchor; 2) the foot then extends and penetrates through the sand with rhythmic probing, and the valves appear to lift up slightly; 3) the hinge muscles contract to close the valves, inducing a high inner pressure that drives body fluids to the foot, causing the distal part of the foot to dilate into a bulbous structure that serves as a terminal anchor; 4) the clam immediately retracts its foot and pulls the valves toward the terminal anchor, resulting in net advancement (Trueman 1966; Trueman et al. 1966a). Using the two anchors—the penetration anchor for the probing process and the terminal anchor for the retraction process—the razor clam is able to propel itself into the ground. Such a simple control strategy and body structure is attractive for engineers to use in designing the next generation of autonomous robotic penetrators for a wide spectrum of applications, such as underground wireless sensing networks, autonomous site exploration, and underground robots.

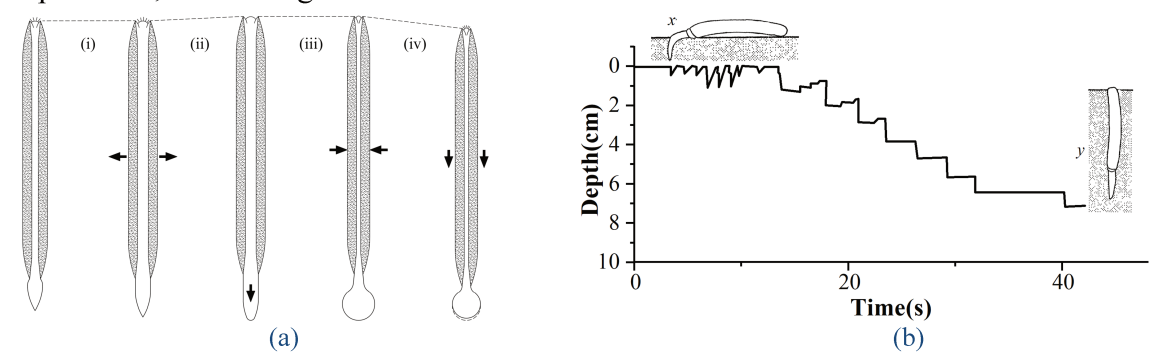


Figure 1. (a) Typical burrowing cycle of the razor clam, where the dotted line denotes the depth and arrows indicate the direction of movement of the foot and valves. (i) Opening of the valves. (ii) The foot probes downward. (iii) Valve adduction pushes body fluids into the foot to form a terminal anchor. (iv) The foot retracts, pulling the valves downward, and the body returns to its initial shape. (b) Depth of burrowing over time (modified from (Trueman 1967)).

Previous studies have found that a juvenile razor clam can dig up to 70 cm into the sand with a maximum body drag force of about 10 N (Holland and Dean 1977; Trueman 1967). However, such a force can only enable quasi-static pushing of a razor clam-shaped aluminum rod into a similar substrate for only around 1 or 2 cm (Winter et al. 2012). In view of soil mechanics, the granular soil will become increasingly loaded with depth under gravitational effects. Normally, the deeper the soil, the more difficult it is to create space for a soft penetrator to move through, and hence a higher resistance will be encountered during penetration. Therefore, such a contradiction between experimental quasi-static penetration and real-life dynamic burrowing indicates that the razor clam must manipulate the surrounding environment during burrowing, leading to reductions in penetration resistance and work. In recent research on burrowing mechanisms and bio-inspired penetrators, (Winter et al. 2014) attributed the high effectiveness and efficiency solely to "localized fluidization" around the clam, which is mainly induced by the closing and uplifting of the shell. These "localized fluidization" phenomena were elegantly explained using a combination of soil mechanics and fluid mechanics, and a robotic clam ("Roboclam") was designed to demonstrate its efficiency (Winter et al. 2014; Winter et al. 2009). Nevertheless, the role of the foot, especially during Stage 2 (extension and probing of the foot) and Stage 3 (foot dilation and anchoring), was not sufficiently addressed. A closer look at the probing foot indicates that while the magnitude of the probing force (~1 N) by the soft foot is relatively small when compared with the retraction force (~10 N) (Trueman 1966; Trueman 1967), the foot is able to penetrate the sediments effectively; furthermore, retraction of the shell occurs in soil that has been highly disturbed by the preceding expansion—contraction of the shell, while the foot is the first part of the clam to penetrate into the area of the soil that is much less disturbed. It was hypothesized that the uplifting movement of the expanded shell contributed to the fluidization of the soil beneath the foot so as to reduce the penetration resistance. However, it was found that the uplifting tendency only occurs during the early stages of self-burying; once the majority of the body has been buried, no further uplifting could be observed (see Fig. 1b). This indicates that for deep penetration, there is barely any fluidization of the soil beneath the foot due to uplifting, and other mechanisms may be in play that enable efficient burrowing. It may also be challenging to rely on localized fluidization for penetration in unsaturated soils and cohesive soils. Therefore, it is beneficial to study the selfburrowing mechanism from new perspectives using new tools, so that the mechanism can be translated into geotechnical engineering terms and applications.

As indicated in (Hosoi and Goldman 2015), two common objective functions are used to characterize the organisms' locomotion: 1) achieving the maximum speed with a given power, which is related to effectiveness; and 2) achieving the highest energy efficiency with a given speed, which is related to efficiency. The former is mainly used in the escaping process, whereas the later used in the foraging or common locomotion process, like anchoring. Organisms in nature tend to flexibly adjust their energy consumptions according to the real situations, instead of sticking to one specific strategy. This indicates that the dynamic burrowing process is a complex process, where influence from the surrounding environment and burrowing kinematics both affect the locomotion performance. To achieve a thorough understanding of the dynamic burrowing mechanism by razor clam is not a trivial task, but it requires systematic research work from different perspectives. The scope of this paper is limited to translating biological burrowing processes into geotechnical terms and evaluating the applicability of two common geomechanics tools in studying clam-inspired dynamic penetration processes.

From a geotechnical engineering and soil mechanics perspective, the burrowing process is

essentially a soil–structure interaction problem and, more fundamentally, a momentum and energy transfer process. The penetration efficiency is governed by the various dissipation mechanisms in the penetration process, such as frictional dissipation (particle-particle, particle-penetrator), viscous drag, kinetic dissipation (agitation of particles) and collisional dissipation. Such dissipation mechanisms depend on 1) the geometry and kinematics of the penetrator and 2) the properties of the granular medium. Soil-structure interactions under quasi-static and dynamic loadings such as those applied in the cone penetration test (CPT) and the responses of buildings/foundations to seismic loading have been studied extensively in recent decades (Gazetas and Makris 1991; Lou et al. 2011; Makris and Gazetas 1992; Stewart et al. 2012; Yu and Mitchell 1998). Rapid penetration of projectiles into granular media has also been studied from a multiscale perspective (Bivin and Simonov 2010; Omidvar et al. 2015). Nearly all penetration phenomena involve stiff intruders that have a stable geometry; moreover, in most studies, the shaft of the intruder has little or no change in curvature. A few studies focus on intruders with nonuniform shapes such groups of bodies (Holland et al. 1990) and deformable bodies (Backman and Goldsmith 1978), but no systematic studies have considered penetration into granular materials by intruders having controlled varying shapes, such as those of burrowing animals. Very limited examples are found in the area of burrowing by biological or robotic bivalves (Germann and Carbajal 2013; Winter et al. 2014; Isava and Winter 2016).

The research described in this paper is a first attempt to model the dynamic burrowing mechanisms from the perspective of geomechanics and to showcase the advantages and limitations of cavity expansion theory and DEM when adopted for modeling the dynamic soil—structure interactions in the burrowing process.

METHODOLOGY

To capture the interactions between the soil and a shape-changing body, common tools in geotechnical engineering such as cavity expansion theory and the discrete element method (DEM) can be employed. The well-established cavity expansion theory has been widely used to interpret various penetration behaviors both for geotechnical engineering purposes and in natural processes. Examples include the interpretation of geotechnical site characterization test results (pressuremeter tests or PMT: (Fahey 1986; Geng et al. 2013); cone penetration tests or CPT: (Salgado 1993; Salgado et al. 1997), studies on the radial growth of plant roots and earthworm burrowing (Ruiz et al. 2016), and most recently evaluation of the potential of self-penetration probes (Martinez et al. 2019). The cavity expansion analysis presented in the previous studies demonstrate the applicability of modeling either a stiff structure with constant geometry interacting with the surrounding soil (e.g., CPT & pile), or a diameter-changing but infinitely long structure interacting with the surrounding soil (e.g., PMT). Nevertheless, very limited research focuses on the cavity expansion analysis of a structure with finite length and time-varying shape interacting with the surrounding soil, such as the case of dynamic burrowing in this study.

On the other hand, DEM has been demonstrated to be a useful alternative technique for the simulation of granular materials. With a basic constitutive law to express the interaction between two contacting phases, DEM can provide us with a macroscopic/microscopic view of the granular response to dynamic perturbation (Cundall and Strack 1979). The DEM modeling approach has been successfully applied to the study of traditional cavity expansion—based penetration behaviors, such as those in CPT ((Arroyo et al. 2011; Butlanska et al. 2013; Falagush et al. 2015), PMT ((Geng et al. 2013) and pile installation (Zhang and Wang 2015); it has also been successfully

implemented to simulate the "swimming behavior" of the common sandfish within a granular material (Maladen et al. 2011). Hence, the DEM modeling approach was implemented here for an illustration of the complex dynamic soil-burrower interaction and the validity of the cavity expansion theory.

Please note that this study is not an attempt to develop an improved DEM or cavity expansion theory, but to apply these two well-demonstrated approaches to a new type of dynamic penetration process, specifically, cyclic dynamic penetration involving shaft expansion and cone penetration. Assumptions and simplifications are typically needed to model the locomotion process of living organisms, since the kinematics and force dynamics of body parts are extremely complex, in addition to the complexity of granular material itself. For example, instead of using a model with a realistic geometry for the sandfish, Ding et al. (2012) used a uniformly shaped, multi-segment model to numerically study the sandfish's highly efficient "swimming" behavior in sand.

Overall Assumptions and Simplifications

Similar to (Jung et al. 2011; Winter et al. 2012), the slender convex shell is simplified as a cylindrical shaft; whereas the muscular foot is simplified as a cone due to the pointy shape during probing. From a geotechnical engineering perspective, the shell-opening feature (Stage *i* in Fig. 1a) is analogous to the pressuremeter test (PMT); while the foot probing feature (Stage *ii* in Fig. 1a) is analogous to the cone penetration test (CPT). In order to capture the key features of the burrowing process, a clam body with a dynamically changing shape was simplified into a two-body penetrator: a conical "foot" and a cylindrical "shell"/shaft with a time-varying diameter. Therefore, the burrowing process of a razor clam is simplified as alternating cycles of PMT and CPT. The dilation and contraction of the foot does not participate in the foot penetration stage and is not included here for the sake of simplicity; however, the effect of foot dilation on the anchorage and retraction stage (Stage *iv* in Fig. 1a) is critical and will be considered in a future study.

Due to a lack of detailed experimental record in the timescale of the clam burrowing process, the kinematics of the penetrator were prescribed so that the diameter of the shaft, the vertical movements of the shaft, and the cone can be controlled separately to model the dynamic burrowing process of the razor clam, and for the sake of implementation of cavity expansion theory and establishing connections with the geotechnical engineering scale. As shown in Fig. 2a, the contraction and expansion of the shell of *Ensis directus* occur gradually and can be approximated using a ramp-step function; between sequential contraction and expansion steps, the minimal and maximal diameters are kept constant for a period of time to allow shell retraction and foot probing, respectively. To simplify the process, we assume that the activities of shell expansion, foot probing, shell contraction, and shell retraction occur consecutively without overlap. We also assume that the velocities for the downward motion of the foot and the retraction of the shell are the same; the shape of the foot is a cone with a diameter of 15.2 mm and an apex angle of 60°; the cone shape is fixed and is not permitted to dilate/contract. Similar to the body of a razor clam, the cylindrical shaft has a length of 86.8 mm and an initial diameter of 15.2 mm; and the shaft is able to expand to a maximum diameter of 18.24 mm, which is equivalent to an expansion ratio of 0.20. The penetrator size is comparable to the size of a typical razor clam (Ensis directus) (Winter et al. 2014); the aspect ratio is consistent with our biological observations. The expansion ratio of 20% is chosen through estimation from the average width change of the shelled body. This ratio is determined using the body width and the average gape angle change (20°) of the two rotating valves from closing to opening (Trueman 1967). The cylindrical shaft expands/contracts linearly

with a constant strain rate of 0.02 at the expansion/contraction stage; at the same time, the penetrating cone and contracted shaft are able to travel vertically at a constant velocity of 2 cm/s. The shaft expansion/contraction rate and the cone penetration rate are comparable with the strain rate in PMT (ASTMD4719-07 2016) and penetrometer advancing rate in CPT (ASTMD3441-16 2016). The choice of these rates is for making analogies with the geotechnical engineering processes. In reality, the razor clam has a shell closing rate of $1.1 \sim 2.8$ cm/s and an average body advancing rate of 1 cm/s (Trueman 1967; Winter et al. 2013).

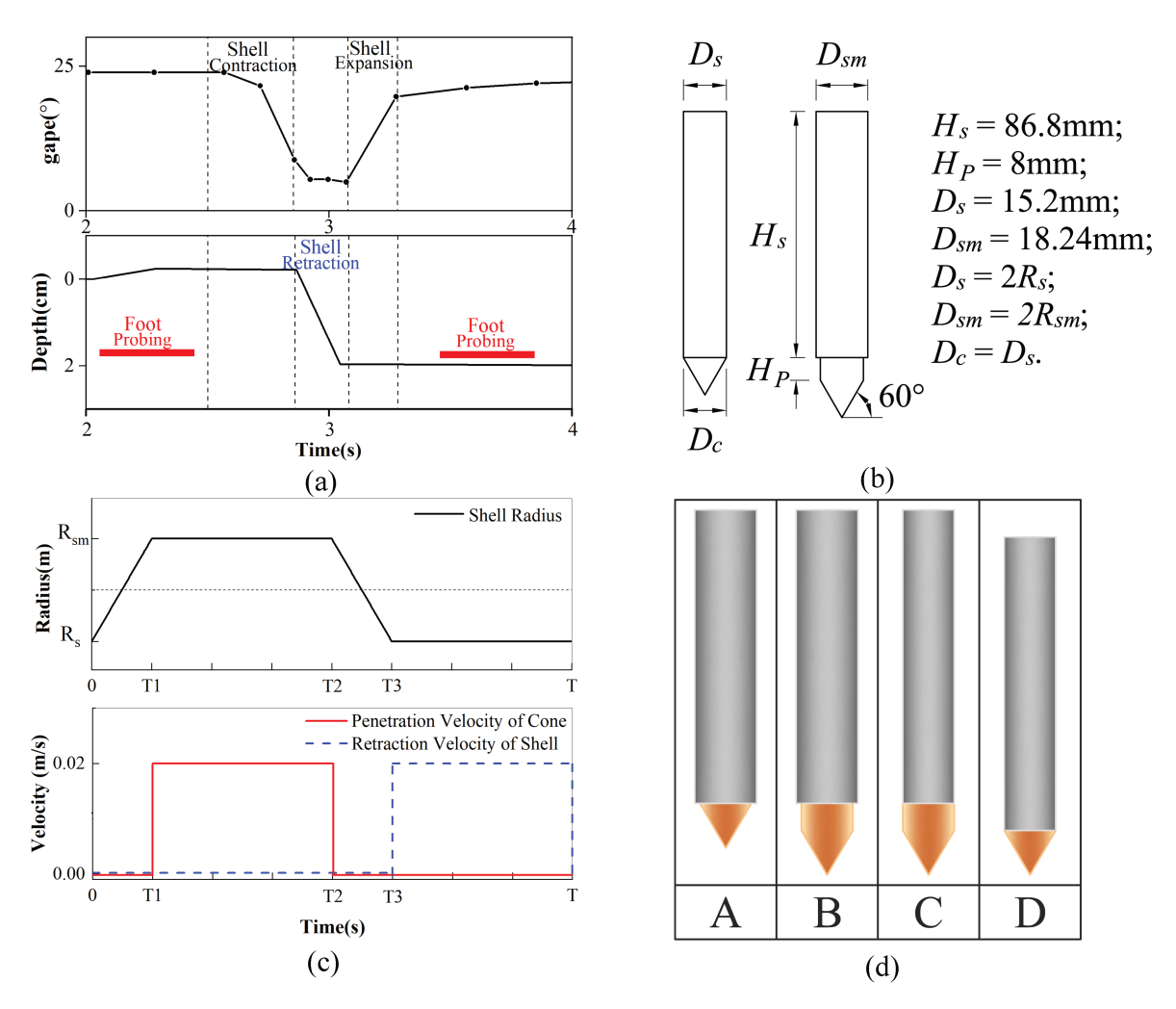


Figure 2. Burrowing kinematics: (a) Burrowing cycle of a living Ensis directus (modified from (Trueman 1967)). The angle between the valves (in degrees) represents shell contraction and expansion, the depth of penetration indicates the shell retraction, and the foot probing process is placed in the correct time sequence. (b) Dimensions of the designed two-body penetrator. (c) The kinematics of the shell and foot are modeled with Eq. (1), which is based on (a). (d) The burrowing cycle of the numerical two-body penetrator, which is based on (c). Stages A: shaft expansion, B: cone penetration, C: shaft contraction and D: shaft retraction

The detailed kinematics of the shaft and cone can be described using Eq. (1). A graphic visualization of the displacement-controlled shape-changing process is shown in Fig. 2c.

$$\begin{cases} R_{shaft} = R_s + \frac{\alpha R_s}{t_e} t &, nT \leq t \leq nT + t_e \\ v_{shaft} = 0.0; v_{cone} = 0.0 \\ R_{shaft} = (1 + \alpha)R_s &, nT + t_e \leq t \leq nT + t_e + t_p \\ v_{shaft} = 0; v_{cone} = 0.02 &, nT + t_e \leq t \leq nT + t_e + t_p \\ R_{shaft} = (1 + \alpha)R_s - \frac{\alpha R_s}{t_c} (t - t_e - t_p) &, nT + t_e + t_p \leq t \leq nT + t_e + t_p + t_c \\ v_{shaft} = 0.0; v_{cone} = 0.0 &, nT + t_e + t_p + t_c \leq t \leq (n + 1)T \end{cases}$$

$$\begin{cases} R_{shaft} = R_s &, nT + t_e + t_p + t_c \leq t \leq (n + 1)T \\ v_{shaft} = 0.02; v_{cone} = 0.0 &, nT + t_e + t_p + t_c \leq t \leq (n + 1)T \end{cases}$$

where

- t is the locomotion time;
- T is the period of a typical locomotion cycle, where $T = t_e + t_p + t_c + t_r$, in which t_e , t_p , t_c and t_r are the duration of shaft expansion, cone penetration, shaft contraction and retraction, respectively. In this study, $t_e = t_c = 0.147$ s and $t_p = t_r = 0.4$ s, which are similar in scale to the durations of the corresponding stages of motion of the razor clam.
- R_s and R_{shaft} are the initial radius and current real-time radius of the shaft, respectively;
- v_{shaft} and v_{cone} are the traveling velocities of the shaft and penetration cone, respectively; and
- α is the expansion ratio (i.e., the ratio of the maximum radius increment of the shaft over its initial radius R_s) and is equal to 0.2.

The soil material used for the modeling work is a dry synthetic soil with uniform spherical particles. A set of particle-scale parameters for the DEM simulations was first determined; a virtual soil sample was generated using DEM; a virtual triaxial test was then conducted to characterize the macro-scale soil parameters, which were then used in the cavity expansion theory-based models. Using the same virtual soil sample, DEM simulations were conducted to model the cone penetration (CP) process, the cylindrical shaft expansion (CE) process, and the coupled dynamic penetration (DP) process with the prescribed kinematics described earlier (these three numerical processes are denoted as DEM-CP, DEM-CE, and DEM-DP, respectively). Similarly, analytical solutions of the cone penetration resistance in the CP process, as well as the shaft expansion pressure in the CE process, were obtained using cavity expansion theory. The DEM-CP results were used to aid the choice of the input soil parameters of the cavity expansion theory models. Next, the penetration forces and energy consumption in the DP processes were calculated using both approaches to ensure comparability (these three analytical models are denoted as ANA-CP, ANA-CE, and ANA-DP, respectively). This approach allowed us to simplify the numerical simulation process and focus on comparing the modeling methods rather than predicting the behaviors. An overview of the process is illustrated in Fig. 3. Additional details about the soil sample and the modeling processes are provided in the subsequent sections.

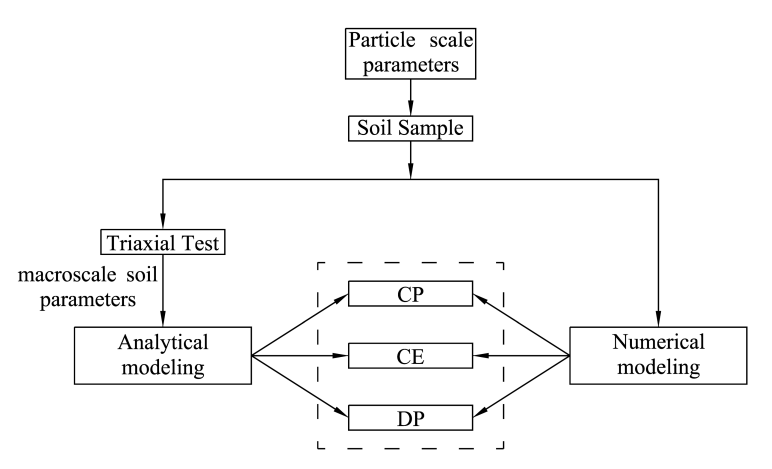


Figure 3. Flowchart showing that the same soil samples were used in both the analytical and numerical modeling approaches. (CP: cone penetration; CE: cylindrical expansion; and DP: dynamic penetration)

Cavity Expansion Theory

Cavity expansion theory is generally concerned with 1) the pressure required to slowly expand a cavity in a medium by a certain amount, or 2) the amount of expansion in a medium induced by a certain level of internal pressure (Yu 2000). Salgado et al. (1997) categorized cavity expansion problems into two cases: a general case and a special case. The general case involves a cavity expanding from a finite initial diameter, while the special case involves a cavity created or expanded from an initial diameter of zero within a medium. The PMT process in a particulate medium is classified as a general case, where an ever-increasing inner pressure is applied to a cylindrical cavity, causing it to expand. A closed form solution for the inner pressure in the general case can be found in (Yu 2000), which is adopted in this study. The CPT process in a particulate environment, on the other hand, is classified as a special case for creating a cavity in the medium. A limit or steady cavity pressure will be achieved once the cavity is created and the medium in the immediate vicinity of the cavity is plastically deformed. The relative size of the plastic zone c over the real-time radius r of the cavity, will also approach a limit (or steady) value in the special case.

A finite element study of a cone penetration test conducted by Huang et al. (2004) suggested that the plastic zones behind the cone and around the shaft are similar to the predictions obtained from the cylindrical cavity expansion model and that the plastic zone around the cone can be assumed to be circular or elliptical in shape (See Fig. 4). Motivated by that study, Yu (2006) assumed that the cone tip resistance can be related to the relative size of the plastic zone through a combination of cylindrical and spherical cavity expansion solutions. To be specific, the cylindrical cavity expansion model is used to estimate the relative size of the plastically deforming zone, and the spherical cavity expansion is then used to determine the cone tip resistance based on the estimated plastic zone size. The procedure is briefly introduced as follows.

The relative size of the plastic zone generated from a cylindrical cavity expanding from a zero initial radius (c/r) was determined by solving the following nonlinear equations for a purely frictional soil (Yu 2000; Yu and Carter 2002):

$$1 = \gamma \left(\frac{c}{r}\right)^{\frac{\alpha - 1}{\alpha}} + (2\delta - \gamma) \left(\frac{c}{r}\right)^{\frac{\beta + 1}{\beta}} \tag{2}$$

$$\alpha = \frac{1 + \sin \phi}{1 - \sin \phi}$$

$$\beta = \frac{1 + \sin \psi}{1 - \sin \psi}$$
(3)

$$\beta = \frac{1 + \sin \psi}{1 - \sin \psi} \tag{4}$$

$$\chi = \frac{(1-v)\alpha p_0'}{(\alpha+1)G} \left[\left(\beta - \frac{v}{1-v}\right) + \frac{1}{\alpha} \left(1 - \frac{v\beta}{1-v}\right) \right] \tag{5}$$

$$s = \frac{\chi(1-\alpha)}{\alpha\beta}$$

$$\gamma = \frac{\alpha\beta s}{\alpha+\beta}$$
(6)
(7)

$$\gamma = \frac{\alpha \beta s}{\alpha + \beta} \tag{7}$$

$$\delta = \frac{(\alpha - 1)p_0'}{2(1+\alpha)G} \tag{8}$$

where p'_0 is the initial effective mean stress, which is 1.0 MPa in this study, and G = E/2(1+v)is the material shear modulus. Other material properties required in the solutions are the elastic modulus E, Poisson's ratio v, friction angle ϕ and dilation angle ψ , which can be determined through a drained triaxial compression test. Once the material properties are determined, the values for $\alpha, \beta, \chi, s, \gamma$ and δ can be obtained, as well as the ratio c/r. The spherical cavity expansion solution is then implemented to determine the cone tip resistance q_c in a purely frictional soil from the relative size of the plastic zone by using the following equation:

$$\frac{q_c}{p_0'} = \frac{3\alpha}{2+\alpha} \left(F\frac{c}{r}\right)^{\frac{2(\alpha-1)}{\alpha}} \tag{9}$$

where F is the plastic zone shape factor, which is taken to be unity for a circular zone around the cone (i.e. $r_{ph} = r_{pv}$ in Fig. 4), or otherwise less than 1.0. The value of F is suggested by (Yu 2006) to be around 0.7 to 0.8, according to the limited large-strain finite element analysis on cone penetration in sand that was conducted by Huang et al. (2004). The best-fit F value for the ANA-CP case was back-calculated according to the steady-state tip resistance from DEM-CP. We consider the back-calculation of the F value as a calibration process. Once the cone tip resistance q_c and the cavity expansion pressure during the dynamic penetration are determined, the corresponding energetic cost per cycle can be estimated by integrating the force along the displacement path.

In order to model the dynamic penetration process with cavity expansion theory, two additional assumptions are made: 1) interdependency among the different steps is disregarded in the model; and 2) the shaft contraction process is regarded as the elastic rebound of the shaft expansion behavior in which no additional energy expenditure is required. Therefore, the cone penetration process and the shaft expansion process during dynamic penetration can be analyzed independently using cavity expansion theory. Finally, in this study, the resultant performance for each burrowing cycle is estimated by simple combination of the four independent steps; the total energy consumption for a typical burrowing cycle is only simple superposition of the energetic costs in the shaft expansion/retraction and the cone penetration, since the dilation/contraction of the foot is neglected.

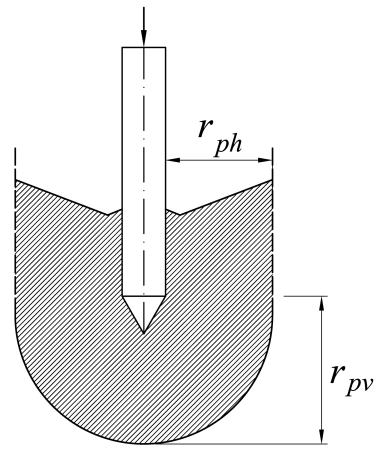


Figure 4. Plastic zone around a cone in sand (Huang et al. 2004).

Numerical Method

Model Construction

A commercial software package, *PFC 3D* (version 5.00.22) was employed for the DEM simulations. In order to reduce the computational demand, the soil particles are modeled as spherical rigid balls; the penetrator/cavity consists of rigid walls, which are composed of a triangular mesh of facets. In *PFC 3D*, the movement of the particles is updated according to Newton's laws of motion; the movement of the faceted penetrator/cavity is achieved by independently assigning a user-defined velocity to each vertex of the triangular facet (Itasca Consulting Group 2015). Interactions among these contacting entities are dictated by contact laws or contact models. Commonly used elastic contact models can be sub-classified into simple linear contact models and nonlinear contact models. In simple linear contact models, the relationship between the contact force and the displacement of the two contacting entities follows a linear law; in nonlinear models such as the Hertz–Mindlin contact model, the contact force–displacement relationship is affected by the sizes of the particles in contact and, thus, follows a nonlinear law. Previous work has shown that the Hertz–Mindlin contact model is able to capture the stress-dependent response of the soil at different strain levels (Zhang and Wang 2015) and is more suitable for dynamic problems. Thus, the Hertz–Mindlin contact model was adopted in this study.

In *PFC 3D*, the built-in nonlinear Hertz–Mindlin contact model is based on an approximation of the theory of (Mindlin and Deresiewica 2013). Additional details about DEM implementation are described in (Cundall 1988). The Hertz–Mindlin contact model is defined by two major particle-scale properties: the shear modulus and the Poisson's ratio of the two contacting entities. To prepare the soil sample, a built-in particle-based local damping scheme was adopted to allow dissipation of the additional kinetic energy of the particles and to establish an equilibrium state within a short period of time. After the sample was prepared, this local damping was removed, and a viscous damping strategy was adopted in the subsequent simulations. Details of the inputs for the particle-scale properties and the contact parameters adopted in the simulation are summarized in Table 1. Please note that in this study, no attempt was made to predict the dynamic soil–structure interactions within a real soil sample; the focus in this study was on facilitating a comparison between the two modeling approaches for the clam-inspired dynamic penetration processes.

Table 1. Simulation Parameters

Particle parameters					
Shear modulus	2.5e8 Pa				
Poisson's ratio	0.3				
Friction coefficient	0.0 (soil deposition)				
Friction coefficient	0.5 (otherwise)				
Wall parameters					
Shear modulus	2.5e8 Pa				
Poisson's ratio	0.3				
E : 4: 0° : 4	0.3 (cone–particle)				
Friction coefficient	0.0 (otherwise)				
Hertz-Mindlin contact model parameters					
Shear modulus	2.5e8 Pa				
Poisson's ratio	0.3				
	0.5 (particle–particle)				
Friction coefficient	0.3 (cone–particle)				
	0.0 (otherwise)				
Normal critical damping ratio	0.7				

To construct the virtual calibration chamber, a few geometrical factors were considered. Physical calibration chamber experiments revealed that the ratio of the chamber to the cone diameter has an effect on the measured penetration resistance (Bolton and Gui 1993; Bolton et al. 1999). Bolton and Gui (1993) recommended that a chamber-to-cone diameter ratio should be no less than 40 for centrifuge cone penetration into a dense sand sample in order to eliminate the boundary effect. On the other hand, Butlanska et al. (2010) found that using a large sample (i.e. one having a chamberto-cone diameter ratio higher than 33) in the numerical test will significantly increase the computational effort and sample inhomogeneity and, hence, will affect the accuracy of final results. The number of contacts between the penetrator and the particles will also affect the accuracy of the DEM simulations. Using a smaller cone-to-particle diameter ratio will cause noticeable oscillations to develop in the tip resistance (Butlanska 2014). A higher accuracy can be achieved by using both a larger chamber-to-cone diameter ratio and a larger cone-to particle diameter ratio. which requires a relatively large sample with relatively small particles. The computational cost, however, is enormously high for such a setup and, consequently, a compromise must be made to reduce the computational cost. In this study, we selected a chamber-to-cone diameter ratio of 18.05, but with a stress-controlled boundary to model the infinite far field; we show later that this treatment does not induce noticeable stress boundary effects in this study. We also used a cone-toparticle diameter ratio of 3.04. Through physical experiments, numerical simulations and analytical analysis, it was observed that for very thin penetrators (low cone-to-particle diameter ratio) in granular materials, the tip resistance is usually higher than that of a thicker penetrator (high cone-to-particle diameter ratio) (Bolton et al. 1999, Lin and Wu, 2012, Wu and Ladjal 2014, Zhuang et al. 2018). Therefore, the low cone-to-particle diameter ratio used in this study is considered as a limitation, especially for the analytical analysis based on cavity expansion theory.

To further reduce the computational cost, the refinement method used in (McDowell et al. 2012) was adopted and the sample was virtually sectioned into two co-axial zones that contain particles of two different sizes (see Fig. 5). The inner zone, which measures 0.28 m in diameter and has the

greatest effect on the cone-particle interactions (McDowell et al. 2012), is composed of smaller particles with a diameter of 5 mm. The outer zone, which is a cylindrical shell zone measuring 0.03 m in thickness, consists of slightly larger particles that are 6 mm in diameter.

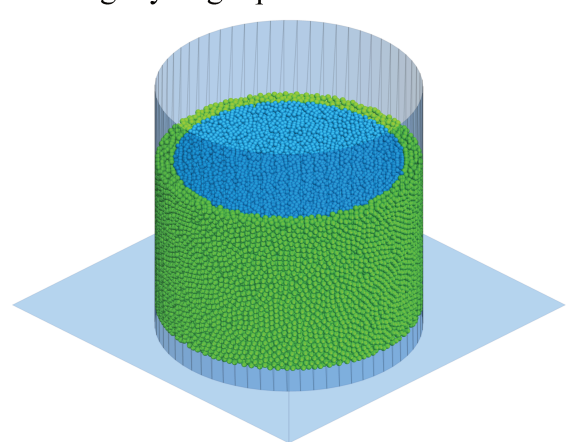


Figure 5. The cylindrical soil sample in the virtual calibration chamber consists two different zones: an inner zone (blue in color) with particles of desired particle sizes and a thin outer zone (green in color) with larger particles.

The soil sample was generated in the virtual calibration chamber using the deposition method, where the particles rained down from the top of the chamber and were freely deposited under the force of gravity to fill the chamber. To prevent particles from migrating between the two zones during particle deposition and the subsequent "consolidation" (isotropic compression) stage, a virtual cylindrical frictionless dividing wall was created in between the two zones. During the deposition process, the frictional coefficient of the soil particles was set to zero to obtain a dense uniform sample; it was reassigned to the target coefficient (0.5) thereafter. An isotropic confining pressure of 1.0 MPa was applied without gravitational effect using a servo control mechanism. The dividing wall was then deleted, and the sample was cycled to quasi-static equilibrium. Although the confining pressure is far beyond the muscle strength of the razor clam, please note that the scope of this study is mainly to illustrate the advantages and limitations of the DEM modeling technique and cavity expansion theory in modeling the dynamic burrowing process inspired by razor clam, rather than to realistically explore the biological burrowing mechanism.

The prepared sample was first used to conduct a drained triaxial test in order to determine the macroscale soil properties for the analytical model based on cavity expansion theory. During the triaxial test, the confining pressure at the lateral chamber wall was maintained at 1.0 MPa, and the axial load was applied by progressively moving the top and bottom boundaries toward the sample center simultaneously under a constant stain rate of 0.02. The same soil sample was then used for the DEM-CP, DEM-CE and DEM-DP simulations, where the top and bottom boundaries were kept fixed and a confining pressure of 1.0 MPa was maintained on the lateral wall boundary. For the DEM-CE case, a cylindrical cavity throughout the sample thickness was created within the sample. The initial cavity radius was adjusted through trial-and-error to achieve an initial state, where the inner pressure and external pressure are both 1 MPa and the final cavity radius after isotropic compression is R_s . The cavity was then expanded at a constant rate. For the DEM-CP and DEM-DP cases, the penetration started from the very top of the soil sample. In addition, the penetration velocities in the DEM-CP and DEM-DP cases, as well as the expansion ratios and the expansion rates in the DEM-CE case and DEM-DP case, were kept the same. Details regarding the parameter values and boundary conditions used in the different simulation stages are summarized in Table 2.

Table 2. Summary of DEM Simulation Stages and Cases

Simulation	Boundary conditions			Particle	Local	Viscous
stages/cases	Тор	Botto m	Lateral wall	friction coefficient	damping ratio	damping ratio
Deposition	free	fixed	fixed	0.0	0.7	0
Consolidation	1.0 MPa confinement			0.5	0.7	0
Triaxial test	Strain control		1.0 MPa confinement	0.5	0	0
DEM-CP	fixed	fixed	1.0 MPa confinement	0.5	0	0.7
DEM-CE	fixed	fixed	1.0 MPa confinement	0.5	0	0.7
DEM-DP	fixed	fixed	1.0 MPa confinement	0.5	0	0.7

Characterization of the penetration process

Several parameters are defined below to aid in discerning the differences between the results from the DEM simulations and those for the cavity expansion theory simulation. Eqs. 10-14 are used for calculations based on the DEM simulations.

1. *Tip resistance*. The tip resistance q_c is the net vertical pressure measured on the conical foot. In DEM, it is expressed in Eq. (10):

$$q_c = \left(\sum_{i=1}^{i=N_c} \left(f_{z,cone}\right)_{i,t}\right) / (\pi r_c^2)$$
(10)

where r_c is the cone radius, N_c is the number of particle—cone contacts at time t, and $(f_{z,cone})_{i,t}$ is the vertical component of the i_{th} contact force applied on the cone surface at time t.

2. Penetration work. The penetration work W_d is defined as the work required for the penetrator to advance its cone with a given velocity for a given period of time, as expressed in Eq. (11):

$$W_d = \int_0^t \sum_{i=1}^{i=N_c} \mathbf{F}_i \cdot d\mathbf{s} = \int_0^t \left(\sum_{i=1}^{i=N_c} \left(f_{z,cone} \right)_{i,t} \right) v_{cone} \cdot dt$$
 (11)

where F_i is the i_{th} contact force (normal and tangential) applied on the cone surface, and ds is the cone displacement for a very short time interval dt.

3. Expansion pressure. The expansion pressure p_t is the net radial pressure applied on the expanding shaft at time t, as described in Eq. (12):

$$p_t = \left(\sum_{i=1}^{i=N_t} \left(f_{n,shaft}\right)_{i,t}\right) / \left(2\pi L R_{shaft}\right) \tag{12}$$

where $(f_{n,shaft})_{i,t}$ is the normal component of the i_{th} contact force applied on the expanding shaft at time t, and L is the depth of the particle—shaft interaction area during body expansion.

4. Expansion work. The expansion work W_e is the work required for the penetrator to expand its cylindrical shaft by a certain amount, as described in Eq. (13):

$$W_e = \int_0^t \left(\sum_{i=1}^{i=N_t} (f_{n,shaft})_{i,t} \right) d(R_{shaft})$$
(13)

5. Retraction work. The retraction work W_r shows the estimation of work required for the penetrator to pull its cylindrical shaft downward by a certain amount, as described in Eq. (14):

$$W_r = \int_0^t \mu_{est} \left(\sum_{i=1}^{i=N_t} (f_{n,shaft})_i \right) v_{shaft} \cdot dt$$
 (14)

where $(f_{n,shaft})_i$ is the normal component of the i_{th} contact force applied on the contracted shaft at time t, and μ_{est} is the estimated frictional coefficient for the particle-shaft interactions, and is equal to 0.3 in this study; v_{shaft} is the vertical retraction rate of the shaft.

Equations for calculating the corresponding metrics based on the cavity expansion theory take similar formats with Eqs. 10-14. Instead of using contact force summations, the force terms are calculated using the expansion-ratio-dependent cylindrical expansion pressure (for W_e), cylindrical cavity expansion limit pressure (for W_r) (Yu 2000) or spherical cavity expansion limit pressure for tip resistance(Yu 2000; Yu 2006) (for W_d).

RESULTS

Soil Parameters

Using the results of the virtual drained triaxial test, it was possible to plot the evolution of the deviatoric stress and the volumetric strain (Fig. 6). As can be noticed from this figure, a pronounced peak deviatoric stress of about 2.06 MPa can be identified at an axial strain of 5.27%. As the vertical strain increased after the peak stress level, the deviatoric stress decreased and approached a relatively constant value of 1.22 MPa. The sample experienced a contraction stage before an axial strain of 3.71%, and it began to dilate after reaching the minimum volumetric strain of -2.22%.

Because no pore pressure was considered in this study, all stress can be considered as effective stress. The vertical axial load σ_a and radial confinement σ_r were the principle stress σ_1 and σ_3 respectively. The elastic modulus E was estimated as the tangent modulus for the axial strain from 0% to 0.5%; the Poisson's ratio v was estimated through the initial strain curve for the strain from 0% to 0.5%. The peak friction angle ϕ_{peak} was selected as the friction angle ϕ ; and it was calculated through the peak stress using Mohr circle of stress. The peak dilation angle ψ_{max} was selected as the dilation angle ψ , which corresponds to the peak strength. Peak state parameters were selected based on suggestions for dense sand under 1 MPa confining pressure (Geng et al. 2013). This is also proven reasonable when calibrating the F value using the DEM-CP results (see below).

These soil parameters were determined via the expressions in Eqs. (15) to (18) (Das 2010; Terzaghi et al. 1996; Vaid and Sasitharan 1992); the calculation results are presented in Table 3. The critical friction angle was also calculated for comparison purpose. These macro-scale parameters were then used in the analytical cavity expansion theory-based model to estimate the cone penetration resistance, expansion pressure, penetration work, and expansion work.

$$E = \frac{\Delta(\sigma_a - \sigma_r)}{\Delta\varepsilon_a} \tag{15}$$

$$E = \frac{\Delta(\sigma_a - \sigma_r)}{\Delta \varepsilon_a}$$

$$\sin \phi = \frac{(\sigma_a - \sigma_r)}{(\sigma_a + \sigma_r)}$$

$$\tan \alpha = 1 - 2n$$
(15)

$$\tan \alpha = 1 - 2v \tag{17}$$

$$\tan \alpha = 1 - 2v \tag{17}$$

$$\sin \psi_{max} = \frac{2}{\frac{3}{|d\varepsilon_v/d\varepsilon_a|} + 1}$$

where ε_a and ε_v are the axial strain and volumetric strain, respectively.

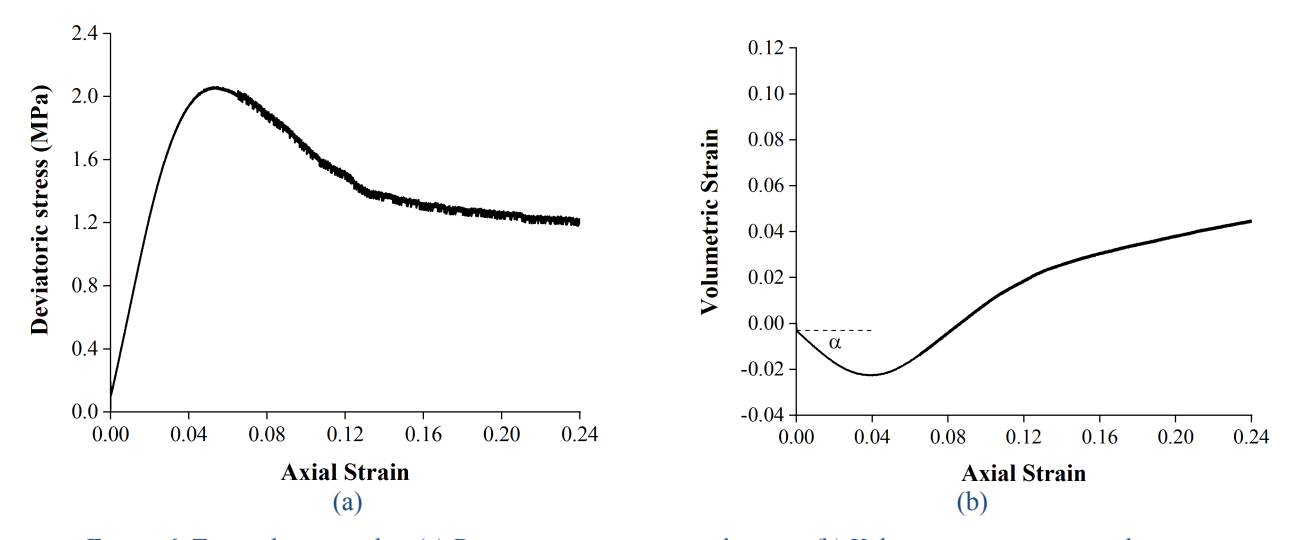


Figure 6. Triaxial test results: (a) Deviatoric stress vs. axial strain. (b) Volumetric strain vs. axial strain.

Table 3. Material Properties for Analytical Solution of Cavity Expansion

Parameter	Value	
Elastic modulus, E	5.63e7 Pa	
Poisson's ratio, <i>v</i>	0.105	
Internal friction angle, ϕ_{peak}	30.2°	
Dilation angle, ψ_{max}	11.7°	
Critical state friction angle, ϕ_{crit}	20.9°	

Cone Tip Resistance, Lateral Pressure on the Shaft and Overall Energetic Cost

To quantitatively study the DEM-DP process, the evolution of the tip resistance q_c was plotted together with the change of the shaft radius over a total of 8 penetration cycles (as shown in Fig. 7a); a single representative dynamic penetration cycle (Cycle 17) was selected to highlight the

change in tip resistance over time (Fig. 7b); the evolution of the lateral earth pressure on the shaft in the same cycle is also included (Fig. 7c). As can be noticed from Fig. 7a, the radial shaft expansion did not contribute to the reduction in tip resistance q_c until the third cycle because it took time to fully submerge the conical tip (0.0132 m long) and because the expanding cylindrical shaft did not interact with the soil at all during the first two cycles. Beginning in the third cycle, a sharp reduction in tip resistance can be observed as the radius of the shaft begins to increase. As can be seen in Fig. 7b, the timing of this reduction in tip resistance coincided with the increase in the shaft radius (i.e., shaft expansion in Segment A in Fig. 7b). Upon the conclusion of the shaft expansion, its radius remained constant while the cone began to penetrate downward (Segment B in Fig. 7b). It is clear that the tip resistance began to increase and eventually exceeded its original value, and then it gradually decreased after the peak value and reached a steady state. The subsequent shaft contraction process (indicated by the reduction of the shaft radius in Segment C in Fig. 7b) and shaft retraction process (Segment D in Fig. 7b) did not affect the tip resistance much. To summarize, shaft expansion causes stress relief at the tip; but this relief is local and temporary. The tip resistance increases again in the subsequent the penetration process after the shaft expansion.

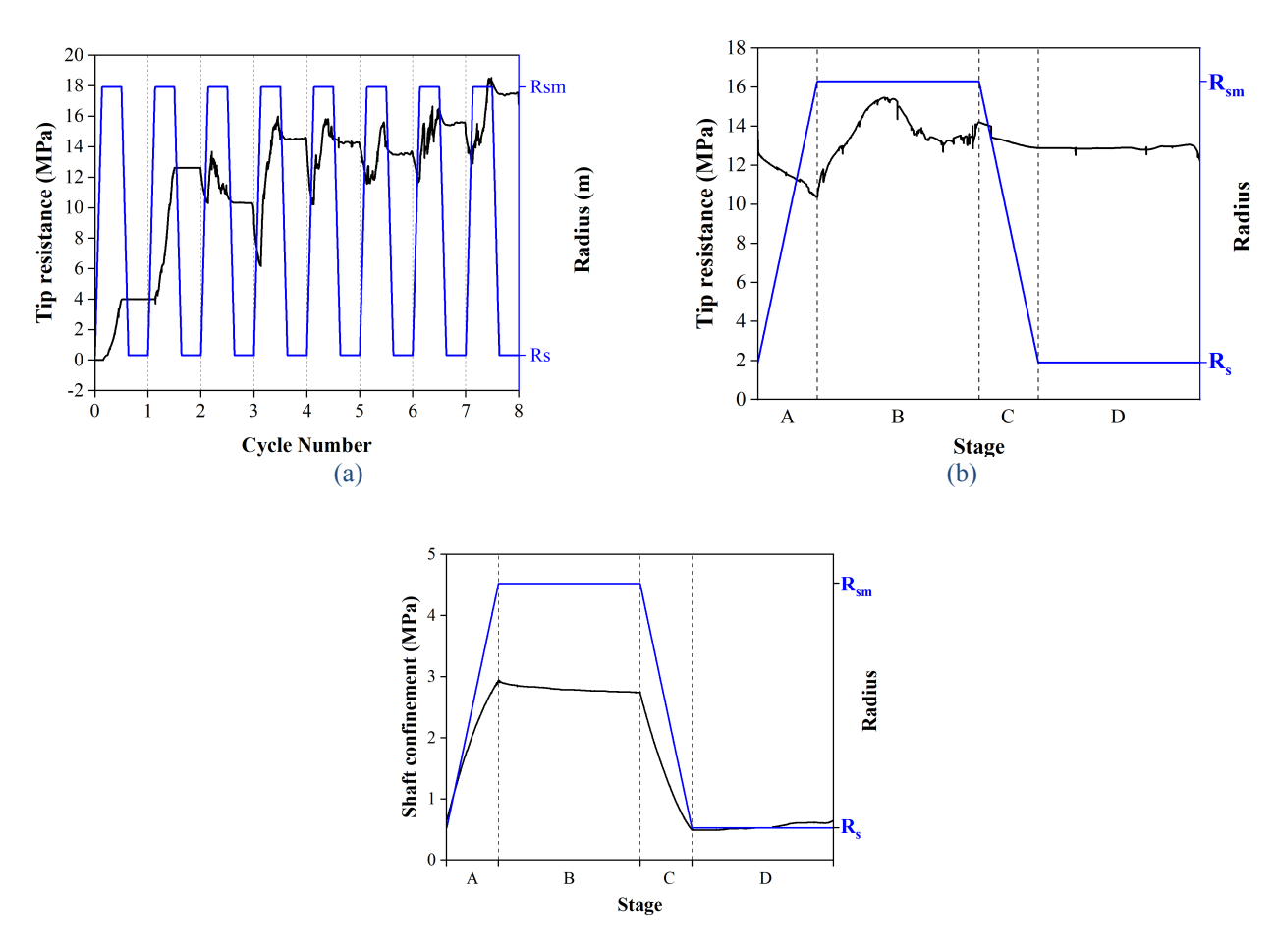
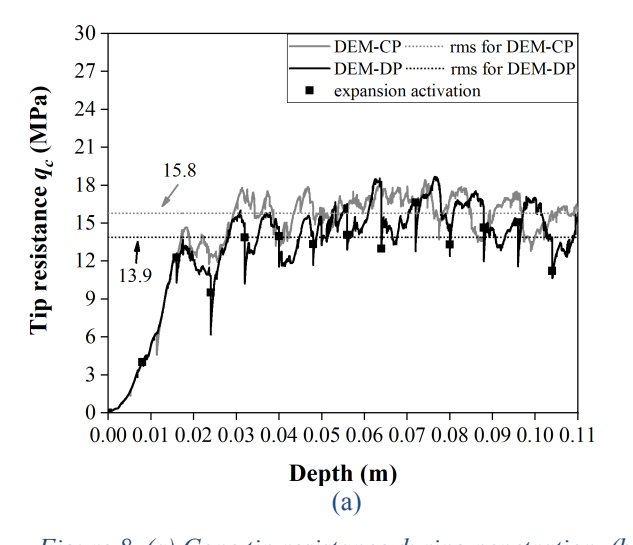


Figure 7. (a) Tip resistance versus cycle number. (b) Tip resistance of each stage in Cycle 17 (at a depth of 0.128 to 0.136 m). (c) Lateral earth pressure on the shaft in Cycle 17.

Significant changes of the lateral earth pressure on the shaft are also observed. Note that at the beginning of the 17th cycle, the average lateral earth pressure on the shaft was lower than the

confining pressure of 1 MPa. In the shaft expansion stage (Stage A), the surrounding soil (not including zones near the top and bottom ends of the shaft) was compressed to a passive state. As a result, the lateral earth pressure increased sharply, which is beneficial for penetration anchor formation. In the cone penetration stage (Stage B), the lateral earth pressure decreased slightly. In the shaft contraction stage (Stage C), the soil was unloaded and lateral earth pressure decreased dramatically to the original level at the beginning of the cycle. This dramatic decrease of the earth pressure is believed to benefit the subsequent shaft retraction process. When the shaft was retracted, a slight increase of the lateral earth pressure can be observed (Stage D).

Fig. 8a shows the analytical and numerical solutions for cone tip resistance during penetration for all cases. In this figure, black dots marked on the q_c curve of the DEM-DP case represent the activation position of shaft expansion. The results obtained for the two numerical penetration simulations are quite noisy with large fluctuations. These noisy fluctuations mostly stem from the discrete nature of the granular particles, dynamic formation and loss of contacts, and soil particle rearrangement around the cone during penetration (Abedi et al. 2012; Falagush et al. 2015). For both the DEM-CP and DEM-DP cases, the cone tip resistance first increases in a nonlinear fashion, but it reaches a steady state after an initial penetration of approximately 0.016 m, where the tip is fully immersed. In order to quantify the difference between the pure cone penetration strategy and the dynamic penetration strategy, the root mean square values of the tip force/resistance from the two strategies at the steady stage (from 0.016 m to 0.11 m) are computed (and are shown in Fig. 8a): 2.87 kN or 15.8 MPa for the DEM-CP case (indicated by the gray dashed line) and 2.53 kN or 13.9 MPa for the DEM-DP case (indicated by the black dashed line).



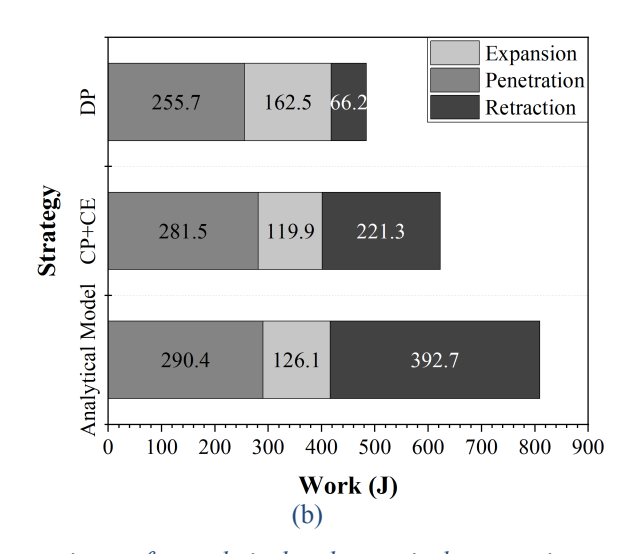


Figure 8. (a) Cone tip resistance during penetration. (b) Energetic cost for analytical and numerical penetration. The first row "DP" indicates the results from the DEM simulation of the dynamic penetration process. The second row "CP+CE" indicates the results from the separate DEM simulations for the cone penetration process and the cavity expansion process. The third row indicates the results obtained from the analytical cavity expansion theory.

For the DEM-DP case, a notable cyclic reduction of the tip resistance was observed to occur after the shaft expansion impact is induced (depth > 0.016 m). Compared to the DEM-CP cases, the reduction in the tip resistance caused by shaft expansion is about 11.9% on average. Such a reduction was maintained during the remainder of the penetration process. This phenomenon underlines the influence of radial shaft expansion on the reduction in tip resistance during the dynamic penetration process. This also indicates that by opening its shell, a razor clam is not only

able to form a penetration anchor, but it can also reduce the foot penetration resistance.

To apply the cavity expansion theory to estimate the tip resistance, the plastic zone shape factor F need to be calibrated. Calibrated using the mean steady state tip resistance of the DEM-CP results and the peak state soil parameters, the best-fit shape factor F for ANA-CP was found to be 0.691, which is comparable to the values (0.7 to 0.8) suggested by Yu (2006). If the critical state parameters were used, the best-fit shape factor F was found to be 1.4, which is not realistic since F should be no greater than 1. This also supports the use of peak state parameters in the analytical model. If back-calculated to match the DEM-DP results, an F value for ANA-DP of 0.629 was obtained. The difference in best-fit F values for the ANA-CP and ANA-DP models may imply that inclusion of body expansion changes the plastic zone shape and results in a reduction of tip resistance. Please note that the back-calculated F for the DEM-DP case is just an attempt to provide an average equivalent fitting, and that the F value may be varied during the dynamic penetration process. A comparison of the back calculated F values is summarized in Table 4.

Index	Friction angle (°)	Dilation angle (°)	Back- calculated F	Analytical solution (MPa)	Calibration case/ (MPa)
1	30.2	11.7	0.691	15.8	DEM-CP/15.8
2	30.2	11.7	0.629	13.9	DEM-DP/13.9
3	20.9	0	1.4	15.8	DEM-CP/15.8

Table 4. Comparison of back calculated F values

The energy consumption required for the penetrator to move from the very top of the sample to a depth of 0.104~m was computed based on Eqs. (11) \sim (14) for the analytical model and numerical penetration model (Fig. 8b). The results for ANA-CP and ANA-CE matched well with the results from the DEM-CP case and DEM-CE case, with a difference of approximately 3.1% and 5.2%, respectively. This implies that the analytical model, although simple, can roughly estimate the tip resistance or the expansion pressure involved in the decoupled DEM-CP and DEM-CE processes, given that the parameters are carefully chosen and calibrated. When cavity expansion theory was used to estimate the retraction energy for the direct cone penetration process (DEM-CP), the estimated energy was much higher (77%, 392.7 J vs. 221.3 J) than that from DEM-CP. A plausible explanation is that the shaft resistance along a penetrating rod degrades with penetration depth due to the unloading of the surrounding soil (Lehane 1992, White and Lehane 2004, Gavin and O'Kelly 2007, Jardine et al. 2009); however, this trend cannot be reflected by the adopted cavity expansion theory model.

When comparing the DEM-DP results to the decoupled DEM-CP and DEM-CE results, it was found that the energy consumption for tip penetration was overestimated by about 9.2%, that for the shaft expansion was underestimated by about 35.5%, and that the shaft retraction process was overestimated by about 70% (66.2 J vs. 221.3J). These differences can be readily explained by the results shown in Fig. 7 and indicate that the decoupled DEM-CP and DEM-CE simulations cannot reflect the soil–structure interactions in a dynamic penetration process.

Overall, the energy consumption simply for the penetration movement (cone penetration and shaft retraction) in a DEM-DP process of 0.104 m (255.7 J + 66.2 J = 321.9 J) is 36% lower than that of

a DEM-CP process (281.5 J + 221.3 J = 502.8 J); with the additional energy cost for the shaft expansion considered, the total energy consumption for a DEM-DP process to penetrate 0.104 m (484.4 J) is still slightly lower (%3.7) than that for a direct cone penetration process (281.5 J + 221.3 J = 502.8 J). This comparison implies that the prescribed kinematics in this study significantly enhances the energy efficiency in the penetration movement, but it comes at a cost for additional shaft expansion; it also indicates that the impact of shaft expansion/contraction over the shaft retraction is much higher than the cone penetration stage. However, by modifying the kinematics, it is possible to find combinations of penetration speed, expansion ratio/rate, and the timing of different events that can lead to a much higher efficiency. Since the objective of this study is to highlight the advantages and limitations of different modeling approaches in the application to the modeling of the dynamic burrowing process, of more interest here are the causes for the discrepancies between the decoupled CP and CE processes and the coupled DP process. To explain this, it is necessary to examine the details of the soil–structure interaction in a DP cycle.

Anatomy of a Locomotion Cycle

One of the advantages of using the DEM modeling approach is that it enables to analyze the soil behavior at multiscale. With multiscale analysis, fundamental mechanisms of macro-scale behaviors can be revealed at micro- or meso- scales. Herein, a representative dynamic penetration cycle (Cycle 17, as shown in Fig. 8b) was selected to further explore the penetration dynamics within the granular material of the DP case. The evolution of the particle displacement field, the force chain, stress evolution and the per cycle energetics are discussed in the following subsections.

Displacement field

Figure 9 shows the soil displacement field corresponding to different penetration stages of the penetrator. The magnitude of the particle displacement is non-dimensionalized by the cone radius. To highlight the influence of different penetration stages on the particle displacement field, different colors are used for the values shown in this figure: values lower than 0.025 are indicated in grey, values higher than 0.07 are indicated in red, and other ranges by colors on the gradient color bar. As shown in Fig. 9, the penetration cycle begins with shaft expansion, which causes deformation of the soil around the penetrator (Fig. 9a). Once the maximum expansion is reached, the extension of the cone is triggered, which lasts until the maximum extension is reached (Fig. 9b). The shaft then contracts until it returns to its initial size (Fig. 9c). Finally, the shaft retracts downward and the penetrator returns to its initial state, in preparation for the next cycle (Fig. 9d). As the shaft cyclically expands and contracts, the granular medium around the shaft is periodically packed and unpacked, and the penetration of the cone and retraction of the shaft also disturbs the surrounding soil.

Immediately after the expansion of the shaft (Fig. 9a), it can be seen that the deformation field around the shaft is not uniform: it is more pronounced in areas closer to the center of the shaft and is reduced in the radial direction. Due to the presence of the top and bottom surfaces of the shaft, local deformations and fabric rearrangement at the two ends are also obvious. This contrasts with the DEM-CE case or analytical CE case, where the length of the cavity can be assumed to be infinitely long so that the deformation field is uniform along the axial direction. Such a fabric rearrangement induces changes in the stress state around the cone (Taboada et al. 2005). The subtle change in the stress state demonstrates the existence of interaction between the shaft expansion and the cone penetration, which eventually leads to a reduction of the tip resistance q_c .

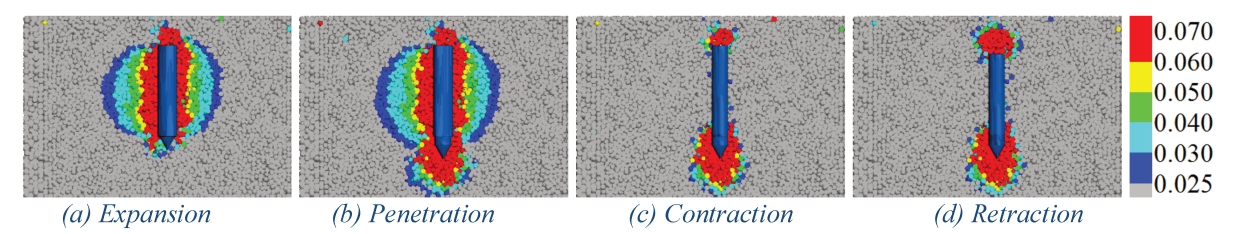


Figure 9. The displacement field of granular particles around the penetrator for different stages of the process. The displacement magnitude of the particle is non-dimensionalized by the initial radius of the cylinder.

The penetration of the tip results in a sectorial deformation area around the cone (Fig. 9b). The extent of the sectorial deformation is slightly attenuated during the processes of shaft contraction (Fig. 9c) and retraction (Fig. 9d). Residual particle displacements along the shaft are present after contraction of the shaft (Fig. 9c), and retraction of the shaft causes the soil above it to collapse, as shown in Fig. 9d.

Contact Force

The contact force chain network is useful in illustrating the force transmission across the entire sample corresponding to each stage in the selected cycle. Relatively strong force chains that carry a large proportion of the stress are generated in the granular material corresponding to different perturbations. In Fig. 10, 3D normal contact force chains are plotted in a planar projection along a vertical section. To properly present and highlight the variability of the force propagation corresponding to each penetration motion, several measures were taken: 1) only the local area around the penetrator is presented in the plots; 2) only forces exceeding 50 N are considered; 3) any forces higher than 400 N are plotted in black; and 4) the lines for the force chains are drawn so that they join at the centroid of the contacting particles, and their thickness is proportional to the magnitude of the force.

As shown in Fig. 10, the strong contact force network clearly concentrates at the vicinity of the cylindrical shaft and the side of the cone, and it diminishes quickly with the increase in distance from the penetrator. In the initial stage, due to the cone penetration and shaft contraction of the previous cycle, an obvious strong force concentration is apparent in the area around the cone, while the force in the area around the shaft is diminished (Fig. 10i). As the shaft expansion proceeds, the strong force chain network around the shaft intensifies, but it decays noticeably in the area around the cone. This obvious contradiction of strong force intensity indicates a release of soil stress around the cone; hence, a smaller tip resistance is applied on the cone during the next cone penetration stage.

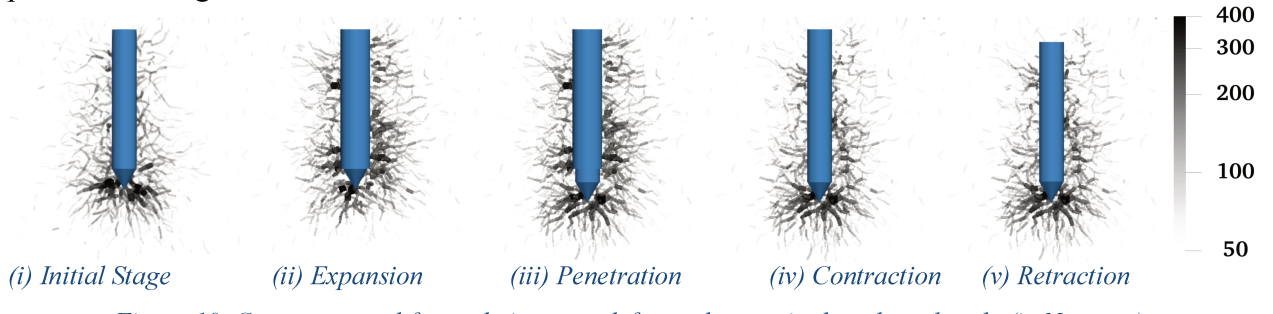


Figure 10. Contact normal force chain network for each stage in the selected cycle (in Newtons).

Differences in the spatial distribution of contact force can be identified in the plots in Fig. 10 during the four-stage locomotion: (1) the strong force network below the cone expands radially and becomes intensified once cone penetration is triggered, and it is maintained until the end of the current cycle; (2) the strong force network become more sparse, with a relatively small force appearing in the vicinity of the shaft at the proceeding stage of shaft contraction. These two differences are consistent with the previous discussion of Fig. 9b–d. In addition, the force network in the vicinity of the shaft during shaft contraction and retraction further affirms that the shaft can be pulled down through the soil with far less lateral stress than the direct penetration case.

Stress Evolution

An influence zone can be defined in different ways. As in this study, it can be defined as the zones with significant (e.g., more than average, or higher than the initial state) changes in average particle displacement or average mean effective stress. To evaluate the extent of the influence zone that is caused by expansion of the shaft, the soil sample was divided into 18 slices (cylindrical shell measurement regions) in the radial direction (Fig. 11a). All measurement regions are co-axial to the chamber and penetrator. The thickness of each measurement region is R_s , the same as the radius of the cone. The influence zone during shaft expansion can then be quantitatively examined through the distribution of the averaged mean effective stress and the averaged non-dimensionalized particle displacement in the measurement regions. Typically, the averaged non-dimensionalized particle displacement is defined as the algebraic mean particle displacement in a representative volume (measurement regions) normalized by the initial shaft radius R_s ; the calculation of the soil stress followed the well-established procedure in (Potyondy and Cundall 2004).

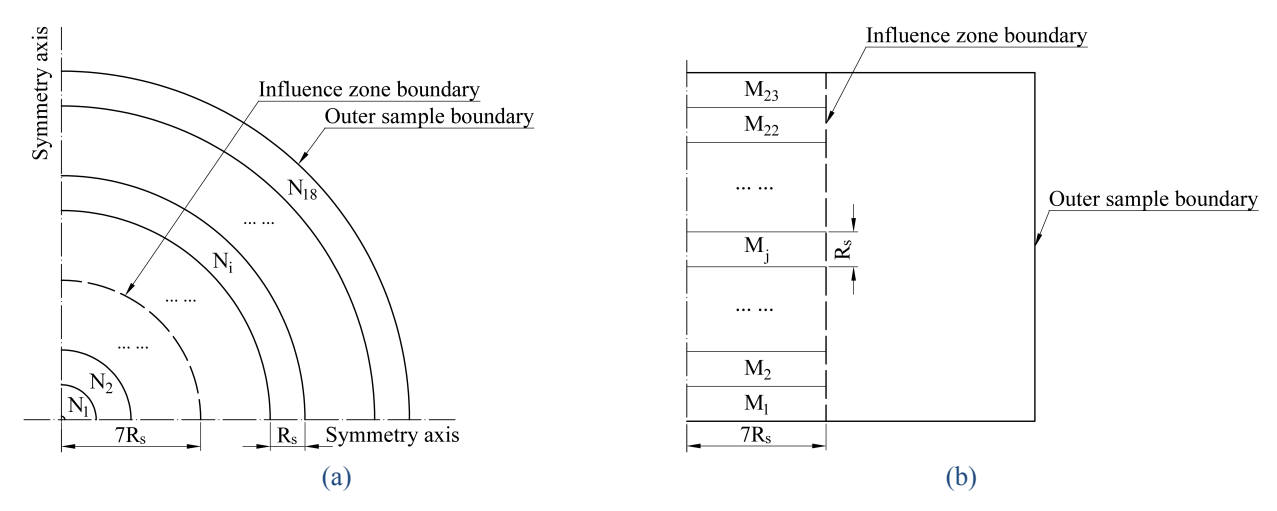


Figure 11. Distribution of the measurement regions: (a) Top view of the measurement regions for the cylindrical shell (only quarter of the sample was displayed due to the symmetry of sample top view). (b) Side view of the cylindrical measurement regions (only half of the sample was presented due to the symmetry of sample side view).

The average particle displacement and stress clearly decrease in the radial direction (Fig. 12). The area of large perturbation (where the normalized displacement values were larger than the average value, 0.015) was limited to a local region within $7R_s$, as measured from the penetrator (Fig. 12a). Such a distribution of displaced particles is consistent with the displacement field shown in Fig. 9a. Fig.12b presents the distribution of mean effective stress in the radial direction of the sample

corresponding to three different stages: 1) the initial isotropic compression stage; 2) at the beginning of the 17^{th} burrowing cycle (or right before shaft expansion); and 3) at the end of shaft expansion for the 17^{th} burrowing cycle. As indicated in Fig.12b, the stress of the soil around the penetrator was changed with the proceeding of the dynamic burrowing. The effect of expansion can be observed by comparing the stress distribution before and after the expansion of the shaft. In the radial direction (Fig. 12b), shaft expansion causes significant stress increase right next to the surface of the penetrator ($R=R_s$). The stress decreases towards both the outer boundary ($R=18R_s$) and the central axis (R=0) of the sample. The expansion effect is noticeable within 5- $6R_s$, which is comparable to the estimation ($5R_s$) from Winter et al. (2014). The vanishing effect at the outer boundary indicates the negligible boundary effects.

The difference between the mean stress distribution of the initial-soil-condition stage and the before-expansion stage indicates that the soil properties around the penetrator are changed after cycles of dynamic cone penetration and cylinder expansion; such changes in the soil stresses cause discrepancy in the prediction using the cavity-expansion based model, which does not consider the loading history during continuous dynamic penetration. The difference between the mean stress distribution before and after the shell expansion stage indicates that the shaft expansion not only causes an obvious stress concentration around the shaft, but also introduces a stress relief to the soil below the cone.

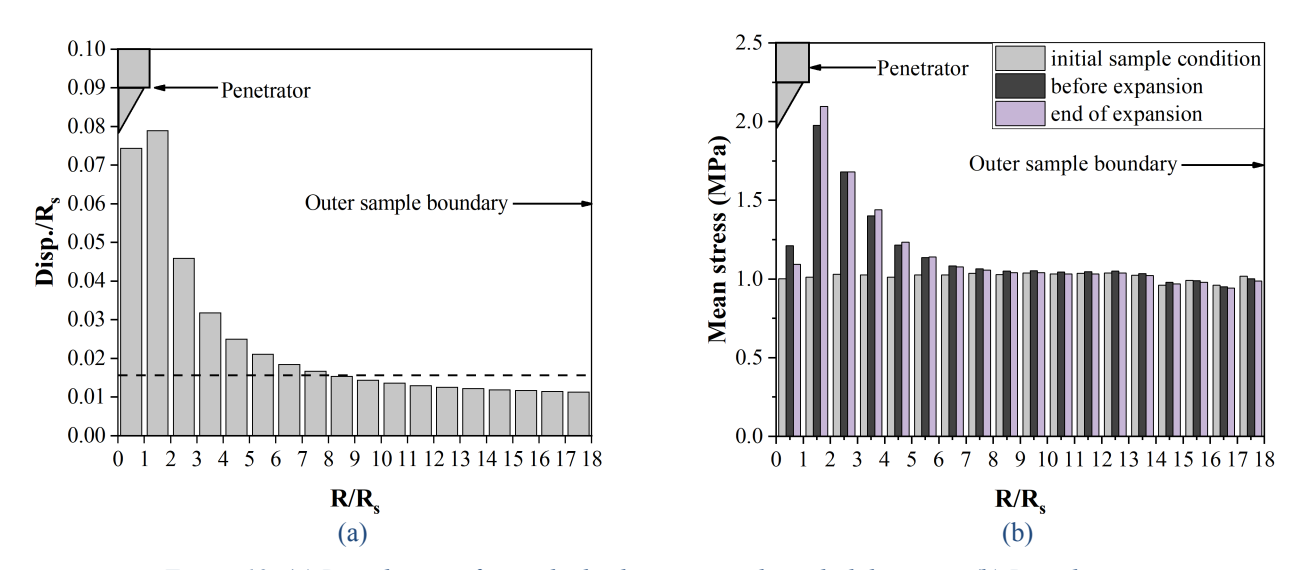
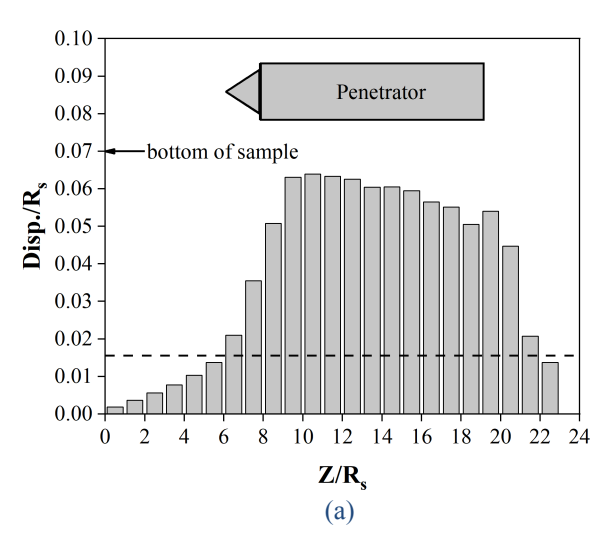


Figure 12. (a) Distribution of particle displacement in the radial direction. (b) Distribution of the average mean effective stress. (Note: The dashed lines indicate the average normalized particle displacement in the entire sample, respectively; the relative location of the penetrator in the radial direction is also shown in the figure for reference).

Similarly, the cylindrical shell regions within the influence zone quantified above was sliced into 23 horizontal discs (each having a diameter of $7R_s$), in order to examine the influence zone in the vertical direction (Fig. 11b). Clearly, the particles around the penetrator were agitated by the radial expansion motion (Fig. 13a); the stress increases within the range of the shaft $(9R_s < Z < 19R_s)$, but decreases towards the top and bottom boundaries ($Z=23R_s$ and $Z=0R_s$) of the sample. The vanishing effects at the top and bottom boundaries indicate that the boundary effect is negligible in the vertical direction. However, the obvious stress relief near the top and bottom ends of the actuators indicates the effect of finite length of the cavity.



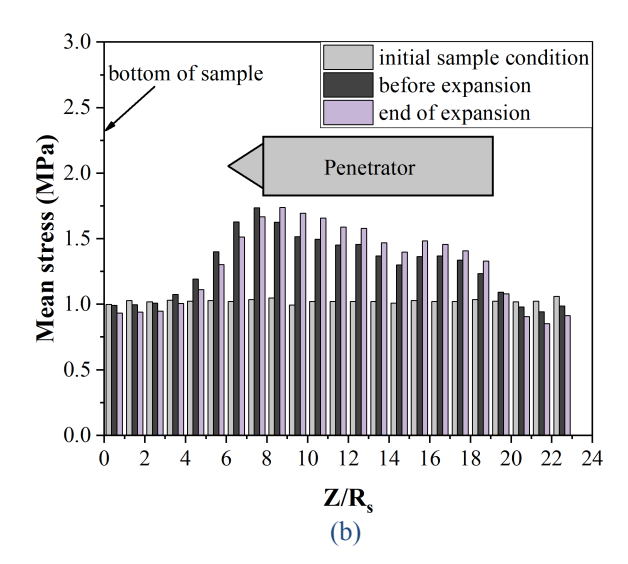


Figure 13. (a) Average particle displacement in the vertical direction. (b) Average mean effective stress in the vertical direction. (Note: The dashed lines indicate the average normalized particle displacement in the entire sample, respectively; the relative location of the penetrator in the axial direction is also shown in the figure for reference).

The mesoscale analysis quantitatively confirms the conclusion drawn from Fig.10. That is, the shaft expansion induces stress relief around the cone and results in a smaller tip resistance in the DEM-DP case comparing to the DEM-CE case.

Energetic Cost in One Cycle

The energetic costs corresponding to each stage in the selected cycle (Cycle 17) are included in Fig. 14a. Based on the DEM-DP simulation, the energy consumption for the shaft expansion and cone penetration motions are 27.8 J and 19.9 J, respectively, in the selected cycle. The ANA-CP penetration work is slightly higher than that from the DEM-DP results. This is consistent with previous conclusions drawn from Figs. 7-13. For the shaft expansion behavior, the expansion work in the DEM-DP case is higher than that of ANA-CE case. Fig. 14b illustrates the evolution of the expansion pressure in the selected penetration cycle (Cycle 17); the DEM-DP result is compared with the DEM-CE and ANA-CE results. As shown in Fig. 14b, the ANA-CE results match well with those for the DEM-CE case; however, the DEM-DP results is significantly higher than that from the analytical estimations. Note that the expansion pressure during cavity expansion largely depends on the properties and stress state of the soil around the cylindrical cavity. The soil properties and confining pressure in the analytical models are assumed to be constant throughout the entire expansion process, while the mechanical properties and the stress state of the soil around the shaft in dynamic penetration vary over time due to the cyclic loading history. The cyclic loading history has changed the soil stress state (Fig. 12b and Fig. 13b), leading to the discrepancies we found between the DP case and the analytical CE case. These discrepancies can also be explained by the contact force chain network shown in Fig. 10.

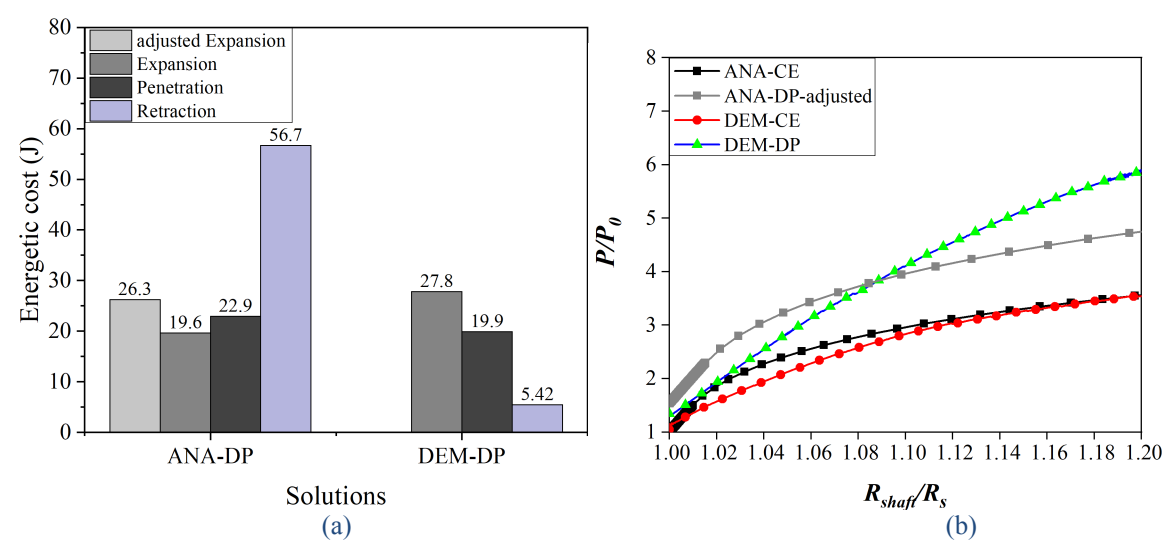


Figure 14. (a) Energetic cost in Cycle 17 (at a depth of 0.128 to 0.136 m). (b) Expansion pressure in Cycle 17 (at a depth of 0.128 to 0.136 m).

Consequently, if cavity expansion theory is still to be used to estimate the cavity expansion pressure in a dynamic penetration case, the confining pressure should be adjusted from the original 1.0 MPa to a higher value. Since the mean pressure along the shaft is not uniform before expansion in the 17th cycle, the average value (1.5 MPa) is used as an adjustment for calculating the expansion curve (Fig.14b). With this adjusted expansion curve, the expansion energy is also updated and shown in Fig. 14a. It's found that the estimations with the adjusted confining pressure match better to the DEM-DP simulation (Fig. 14a and 14b).

Impacts on Shape Factor F for Tip Resistance Estimation

In DEM, the plastic behavior of the soil can be roughly illustrated through the distribution of sliding particle-to-particle contacts. Fig. 15 presents the distribution of sliding contacts around the advancing cone at the cone penetration distance of 0.11m for both DEM-CP and DEM-DP cases. Obviously, different penetration strategies lead to different sliding regions around the cone. Following the sketch in Fig. 4, the sliding zone around the cone for the DEM-CP case tends to have a larger r_{pv} than r_{ph} ; whereas the sliding zone for the DEM-DP case has a much larger r_{ph} than r_{pv} . It is also worthy to note that the sliding zone around the cone for the DEM-DP case is significantly larger than that of the DEM-CP case. In the DEM-CP case, the sliding zone is only locally distributed around the advancing cone. This localization of sliding zone is consistent with the findings from (Huang et al. 2004), which showed that higher mean effective stress and deeper penetration distance result in more localized plastic zone around the cone. However, by incorporating the cylinder expansion into the penetration process, a much wider sliding zone is created around the advancing cone. This observation indicates that the expansion of the shaft introduces changes to the fabric and stress of the soil around the cone; the yield strength for the soil around the cone is reduced and the soil is easier to be disturbed compared with the DEM-CP case. The difference in sliding zone suggests that a different F value should be used to capture the

expansion effect on tip resistance if the cavity expansion is to be used for modeling dynamic burrowing processes. This analysis also provides a potential explanation for the different best-fit F values for the tip resistances in DEM-DP and DEM-CP cases (Table 4).

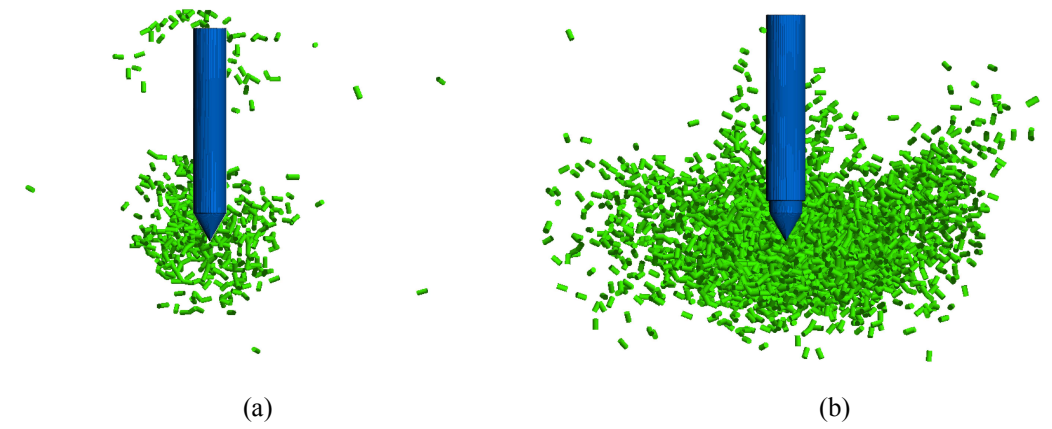


Figure 15. The slipped particle-particle contacts around the penetrator at the cone penetration depth of 0.11m. (a)

Cone penetration case (DEM-CP) (b) Dynamic penetration case (DEM-DP).

DISCUSSION

Modeling approaches

Analytical approaches such as cavity expansion theory are straightforward and easy to implement, as they consider only a few macroscale soil parameters. With carefully chosen and calibrated parameters, one can obtain expansion pressure and penetration resistance quickly and easily, but nothing more. As such, an analytical approach can be a great tool to obtain an order-of-magnitude estimation of force requirements in the conceptual design of a penetration system (e.g., in Martinez et al. 2019). It can also be used to back-calculate the stiffness and strength of the soil, similar to the processes commonly used for interpreting CPT and PMT results. However, the analytical approaches require an expandable shaft that is sufficiently long and demand a situation where there is no or minimal interference between the shaft expansion and cone penetration. Cavity expansion theory assumes that the cavity is infinitely long, so there is no end boundary effect in the axial direction. However, for the natural burrowers and the envisioned self-burrowing robots, the expanding bodies have a finite length and are connected to penetrating body parts. Analytical approaches cannot capture the boundary effects at the end of the expanding bodies or the interactions between an expanding body and a penetrating part, as illustrated by experimental results on the impact of the finite cavity length in pressuremeter tests (Ajalloeian and Yu 1998). It is possible to develop new or modified cavity expansion theories by considering these boundary effects. For example, a generic cavity expansion theory can be developed to consider an expanding body having any shape. Currently, the cavity expansion theory is mainly concerned with two idealized shapes: an infinitely long cylinder or a sphere. Recent developments in cavity expansion theory have considered other shapes, such as an ellipsoid (Zhou et al. 2014). The scenario that uses a finite-length expanding cylinder can be assumed to be an intermediate stage between an expanding cylinder of infinite length and an expanding sphere—or it might be approximated by an expanding ellipsoid. In addition, cavity expansion theory may not capture the partial mobilization effect caused by short penetration depths (White and Bolton 2005), as in the dynamic penetration processes in this study. In order to better predict the dynamic penetration process using analytical cavity expansion theory, extra correction factors considering the shell/shaft-foot/cone interactions should be included. As an example, a pressure value corresponding to the original soil confining pressure is more suitable to be used as the confining pressure on the shell/shaft during the retraction process, than the cavity expansion limit pressure as used in Fig. 8. However, an analytical model that reflects the dynamic interactions between a shape-changing body and the surrounding soil has not yet been developed.

The DEM, on the other hand, enables multi-scale investigations of the soil–structure interactions, but it requires more computing resources than the analytical approaches. By selecting more appropriate constitutive models, particle sizes and shapes, one can improve the accuracy of the simulation results, but it comes at the cost of a much higher computing demand. DEM is ideal to use for exploring the fundamental mechanism of soil–structure interaction with a scaled-down model. However, it is less useful for large-scale systems or for optimization purposes. In order to predict realistic dynamic penetration behaviors, the DEM model should be rigorously calibrated, which itself is a non-trivial task, and the DEM parameters should be calibrated for each soil type. Previous studies showed that even for a single soil type, a set of calibrated and validated parameters under certain boundary loading conditions may not provide equivalently accurate predictions on the soil behavior under different boundary and loading conditions.

Another option for modeling and optimizing the dynamic penetration process is to use continuum-based numerical approaches such as the finite element method and the finite difference method. These approaches typically involve constitutive models (usually nonlinear) to represent the linear elastic, nonlinear plastic and plastic behaviors of soil. Since the cavity expansion boundary value problem involves large strain and dilatant materials, it calls for advanced constitutive models that have been very challenging to establish (Bienen et al. 2012).

Limitations and future needs

This study only focuses on a comparison of different modeling approaches for a penetration system. The real challenges in robotic design will be in optimizing the effectiveness and efficiency of self-burrowing mechanisms. Effectiveness can be quantified by penetration depth per burrowing cycle, which depends very much on the effectiveness of the anchorage. With insufficient anchorage, a burrower may move in a opposite direction than expected, causing slip and ineffective penetration. Efficiency, on the other hand, can be quantified either by penetration velocity per penetration depth or by energy consumption per penetration depth. If penetration velocity is of the utmost importance (for example, in a case where a clam is escaping predators), it is necessary to optimize the penetration velocity; however, most of the time, such a strategy is not the most energy-efficient one. A good analogy to this tradeoff is to consider a runner: a sprinter runs fast over a short distance but expends an enormous amount of energy, while a marathon runner conserves energy by running more slowly over a much longer distance. Which objective function to use for optimization really depends on the application.

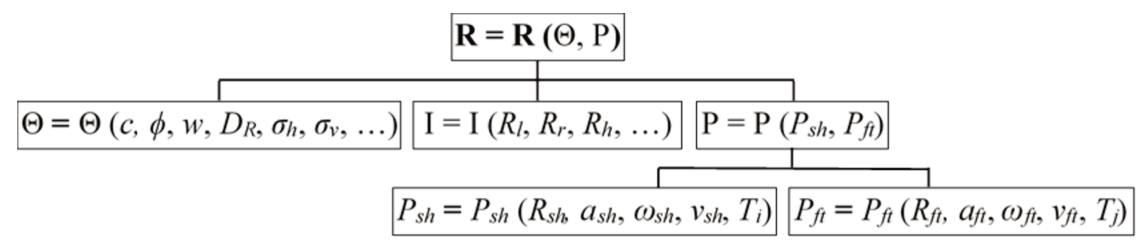


Figure 15. Hierarchical structure of the parameters governing the soil—burrower interaction. Note that the sets of parameters describing the kinematics of the shell and the foot are presented separately; for live clams, however, the kinematics may be correlated and, thus, the total number of parameters can be reduced.

In a general form, the soil-burrower interaction response **R** (characterized by penetration resistance, penetration work, etc.) depends on the soil properties Θ , penetrator kinematics P, and the soil-penetrator interaction conditions I (Fig. 15). Soil properties affecting the interactions can include cohesion c, friction angle ϕ , relative density D_R , and stress state (σ_h and σ_v); the kinematics of the penetrator includes those for the shell P_{sh} and the foot P_{fh} , each of which is governed by its own parameter sets including initial shape (R_{sh} , R_{fl}), final shape (a_{sh} , a_{fl}), shape changing rate/frequency (ω_{sh} , ω_{fl}), and penetration/retraction velocity (v_{sh} , v_{fl}) as well as the duration for each activity T_i (where subscript i indicates shell movements including opening, closure, and retraction) and T_j (where subscript j indicates foot movements including dilation, contraction and penetration); while the soil-penetrator conditions contains the soil-penetrator interface friction R_l , the relative roughness of the soil-penetrator interface R_r , and the relative stiffness of the interface R_h and etc. The Eq. (1) considers only one particular form of burrowing kinematics with some assumptions and simplifications. As the results showed, with the kinematics for this particular burrowing process, the burrowing energy consumption is only slightly lower than that for pure cone penetration.

Furthermore, the soil sample in this study is also significantly simplified. It is acceptable and necessary to use simplified soil samples to explore the multi-scale dynamic soil–structure interactions at the early stages. However, more realistic soil properties are needed to better understand the fundamental mechanisms. The cone-to-particle diameter ratio adopted in this study is relatively low comparing due to the scaling-up of the particle sizes. Zhuang et al (2018) developed a modified version of cavity expansion theory which can consider size effects. It's worthy implementing the improved theories for analytical analysis. With a parametric study that considers different combinations of parameters from Fig. 15, it is possible to optimize the burrowing kinematics for different types of soil. But again, a modeling approach that is efficient and sufficiently accurate is needed to expedite the process.

Another limitation of the current study is that the kinematics of the burrowers is predefined so that the simulation is displacement controlled. It is arguable whether such an approach can precisely reflect the true interactions between the soil and a living organism, whose movement might be dictated mainly by force. Parallel simulations should be conducted to compare both approaches. Furthermore, experimental validation of the findings is also necessary and is currently being explored. This effort requires the development of bioinspired penetrators having similar kinematics to those of the biological models. Eventually, we aim to develop self-burrowing robots, which can be potentially applied many fields including *in-situ* geotechnical testing/mapping, underground sensing networks for precision agriculture or contamination monitoring, targeted

release of mediation agents, underground activity surveillance, and even extraterrestrial exploration, to name just a few.

CONCLUSIONS

Bio-inspired geotechnics, as an emerging subdiscipline of geotechnical engineering, explores how geotechnical engineers can learn from nature to improve the sustainability, resilience and smartness of the tools and methods in geotechnical practice. This paper introduces a new bio-inspired geotechnics topic on self-burrowing robots. To more effectively introduce this concept to the geotechnical community, we explored analogies between the penetration characteristics of a razor clam and *in-situ* exploration methods (i.e., CPT and PMT). We adopted methods commonly used in geotechnical engineering (i.e., cavity expansion theory and DEM) to provide a new perspective to better understand the interactions between dry sand and a two-body, shape-changing structure (i.e., an expandable shaft and a cone), whose kinematics was inspired by that of the razor clam. Some key findings from this preliminary study include the following:

- 1) Cavity expansion theory can be used to reasonably predict the decoupled cone penetration and cavity expansion responses for infinitely-long penetrators, given that the parameters are carefully chosen and calibrated.
- 2) Cavity expansion theory has limitations for predicting a dynamic penetration process that includes coupled cylindrical shaft expansion and cone penetration. The reasons for this limitation can be classified into two main aspects: i) in the coupled process, the shaft is limited in length, and the boundary conditions at the two ends violate the assumptions of cavity expansion theory; and ii) the cyclic expansion—contraction movements cause changes in the soil fabric and force distributions along the shaft that also violate the assumptions of cavity expansion theory.
- 3) DEM simulations reveal the particle-scale changes of the displacement and contact forces, which can be used to explain the fundamental mechanism of the interactions between granular materials and a dynamically shape-changing structure.
- 4) Expansion of a finite-length cavity causes local stress relief at the position of the cone, which leads to a reduction in the tip resistance when the penetration by the cone is initiated; however, this reduction is temporary, and the tip resistance increases again with a further increase in the penetration depth.
- 5) Contraction of the shaft reduces the contacting pressure on the shaft, which leads to a reduction in the shaft resistance when the shaft is retracted.

The energy consumption of the dynamic penetration with selected kinematics is only slightly lower than that for pure cone penetration. By changing the kinematics and incorporating foot anchorage and other burrowing mechanisms (such as vibration and water jetting), it is possible to achieve self-burrowing mechanisms that are highly effective and efficient.

ACKNOWLEDGEMENT

This material is based upon work supported by the National Science Foundation (NSF) under NSF CMMI 1849674. The authors also would like to thank program manager Dr. Richard Fragaszy for his support. Any opinions, findings and conclusions or recommendations expressed in this material are those of the authors and do not necessarily reflect those of the NSF. The authors also would like to thank the two anonymous reviewers, whose comments and suggestions greatly helped us

improve the overall quality of the paper.

REFERENCES

- Abdalla, A., Hettiaratchi, D., and Reece, A. (1969). "The mechanics of root growth in granular media." *Journal of Agricultural Engineering Research*, 14(3), 236-248.
- Abedi, S., Rechenmacher, A. L., and Orlando, A. D. (2012). "Vortex formation and dissolution in sheared sands." *Granular Matter*, 14(6), 695-705.
- Ajalloeian, R., and Yu, H. (1998). "Chamber studies of the effects of pressuremeter geometry on test results in sand." *Geotechnique*, 48(5), 621-636.
- Arroyo, M., Butlanska, J., Gens, A., Calvetti, F., and Jamiolkowski, M. (2011). "Cone penetration tests in a virtual calibration chamber." *Geotechnique*, 61(6), 525-531.
- ASTMD3441-16 (2016). "Standard Test Method for Mechanical Cone Penetration Testing of Soils." ASTM International.
- ASTMD4719-07 (2016). "Standard Test Method for Prebored Pressuremeter Testing in Soils." ASTM International.
- Backman, M. E., and Goldsmith, W. (1978). "The mechanics of penetration of projectiles into targets." *International Journal of Engineering Science*, 16(1), 1-99.
- Bienen, B., Gaudin, C., Cassidy, M. J., Rausch, L., and Purwana, O. A. (2012). "Numerical modelling of undrained capacity of hybrid skirted foundation under combined loading." *International Journal of Offshore and Polar Engineering*, 22(04).
- Bivin, Y. K., and Simonov, I. (2010). "Mechanics of dynamic penetration into soil medium." *Mechanics of Solids*, 45(6), 892-920.
- Bolton, M., and Gui, M. (1993). The study of relative density and boundary effects for cone penetration tests in centrifuge, University of Cambridge, Department of Engineering.
- Bolton, M. D., Gui, M.-W., Garnier, J., Corte, J. F., Bagge, G., Laue, J., and Renzi, R. (1999). "Centrifuge cone penetration tests in sand." *Géotechnique*, 49(4), 543-552.
- Butlanska, J. (2014). "Cone penetration test in a virtual calibration chamber."
- Butlanska, J., Arroyo, M., and Gens, A. (2010). "Size effects on a virtual calibration chamber." *Numerical methods in geotechnical engineering. Edited by T. Benz and S. Nordal. CRC Press, Balkema*, 225-230.
- Butlanska, J., Arroyo, M., Gens, A., and O'Sullivan, C. (2013). "Multi-scale analysis of cone penetration test (CPT) in a virtual calibration chamber." *Canadian Geotechnical Journal*, 51(1), 51-66.
- Cundall, P. (1988). "Computer simulations of dense sphere assemblies." *Micromechanics of granular materials*, 4, 113-123.
- Cundall, P. A., and Strack, O. D. (1979). "A discrete numerical model for granular assemblies." *Geotechnique*, 29(1), 47-65.
- Das, B. M. (2010). Principles of Geotechnical Engineering, 7th Edition, Cengage Learning.
- Ding, Y., Sharpe, S. S., Masse, A., and Goldman, D. I. (2012). "Mechanics of undulatory swimming in a frictional fluid." *PLoS Comput Biol*, 8(12), e1002810.
- Dorgan, K. M. (2015). "The biomechanics of burrowing and boring." J Exp Biol, 218(Pt 2), 176-183.
- Elbaum, R., Zaltzman, L., Burgert, I., and Fratzl, P. (2007). "The role of wheat awns in the seed dispersal unit." *Science*, 316(5826), 884-886.
- Fahey, M. (1986). "Expansion of a thick cylinder of sand: a laboratory simulation of the pressuremeter test." *Geotechnique*, 36(3), 397-424.
- Falagush, O., McDowell, G. R., Yu, H. S., and de Bono, J. P. (2015). "Discrete element modelling and cavity expansion analysis of cone penetration testing." *Granular Matter*, 17(4), 483-495.
- Gazetas, G., and Makris, N. (1991). "Dynamic pile soil pile interaction. Part I: Analysis of axial vibration." *Earthquake Engineering & Structural Dynamics*, 20(2), 115-132.

- Gavin, K. and O'Kelly, B. (2007) "Effect of Friction Fatigue on Pile Capacity in Dense Sand". *Journal of Geotechnical and Geoenvironmental Engineering* 133(1): 63-71.
- Geng, Y., Yu, H., and McDowell, G. (2013). "Discrete element modelling of cavity expansion and pressuremeter test." *Geomechanics and Geoengineering*, 8(3), 179-190.
- Germann, D., and Carbajal, J. P. (2013). "Burrowing behaviour of robotic bivalves with synthetic morphologies." *Bioinspiration & biomimetics*, 8(4), 046009.
- Holland, A., and Dean, J. (1977). "The biology of the stout razor clamTagelus plebeius: I. Animal-sediment relationships, feeding mechanism, and community biology." *Chesapeake Science*, 18(1), 58-66.
- Holland, P., Gordon, J., Menna, T., and Charters, A. (1990). "Hydrocode results for the penetration of continuous, segmented and hybrid rods compared with ballistic experiments." *International Journal of Impact Engineering*, 10(1-4), 241-250.
- Hosoi, A. E., and Goldman, D. I. (2015). "Beneath Our Feet: Strategies for Locomotion in Granular Media." *Annual Review of Fluid Mechanics, Vol 47*, S. H. Davis, and P. Moin, eds., Annual Reviews, Palo Alto, 431-453.
- Huang, W., Sheng, D., Sloan, S., and Yu, H. (2004). "Finite element analysis of cone penetration in cohesionless soil." *Computers and Geotechnics*, 31(7), 517-528.
- Isava, M., and Winter, A. G. (2016). "Razor clam-inspired burrowing in dry soil." *International Journal of Non-Linear Mechanics*, 81, 30-39.
- Itasca Consulting Group, I. (2015). "Guide book: theory and background PFC3D."
- Jardine, R. and Yang, Z. (2013) "Measurement of stressess around closed-ended displacement piles in sand", *Geotechnique*, DOI: 10.1680/geot.9.P.137
- Jung, S., Winter, A. G., and Hosoi, A. (2011). "Dynamics of digging in wet soil." *International Journal of Non-Linear Mechanics*, 46(4), 602-606.
- Lehane, B. M. (1992). "Experimental investigations of pile behavior using instrumented field piles." Ph.D. thesis, University of London Imperial College, London.
- Lin, J., and Wu, W. (2012). "Numerical study of miniature penetrometer in granular material by discrete element method." *Philosophical Magazine*, 92(28-30), 3474-3482.
- Lou, M., Wang, H., Chen, X., and Zhai, Y. (2011). "Structure–soil–structure interaction: Literature review." *Soil Dynamics and Earthquake Engineering*, 31(12), 1724-1731.
- Makris, N., and Gazetas, G. (1992). "Dynamic pile soil pile interaction. Part II: Lateral and seismic response." *Earthquake engineering & structural dynamics*, 21(2), 145-162.
- Maladen, R. D., Ding, Y., Umbanhowar, P. B., and Goldman, D. I. (2011). "Undulatory swimming in sand: experimental and simulation studies of a robotic sandfish." *The International Journal of Robotics Research*, 30(7), 793-805.
- Maladen, R. D., Ding, Y., Umbanhowar, P. B., Kamor, A., and Goldman, D. I. (2011). "Mechanical models of sandfish locomotion reveal principles of high performance subsurface sand-swimming." *Journal of The Royal Society Interface*, 8(62), 1332-1345.
- Martinez, A., DeJong, J. T., Jaeger, R. A., and Khosravi, A. (2019). "Evaluation of Self-Penetration Potential of a Bio-Inspired Site Characterization Probe by Cavity Expansion Analysis." *Canadian Geotechnical Journal* DOI: 10.1139/cgj-2018-0864.
- McDowell, G. R., Falagush, O., and Yu, H. S. (2012). "A particle refinement method for simulating DEM of cone penetration testing in granular materials." *Geotechnique Letters*, 2, 141-147.
- Mindlin, R. D., and Deresiewica, H. (2013). "Elastic spheres in contact under varying oblique forces." *Journal of applied mechanics*, 20.
- Omidvar, M., Malioche, J. D., Bless, S., and Iskander, M. (2015). "Phenomenology of rapid projectile penetration into granular soils." *International Journal of Impact Engineering*, 85, 146-160.
- Potyondy, D., and Cundall, P. (2004). "A bonded-particle model for rock." *International journal of rock mechanics and mining sciences*, 41(8), 1329-1364.
- Ruiz, S., Straub, I., Schymanski, S. J., and Or, D. (2016). "Experimental Evaluation of Earthworm and Plant Root Soil Penetration—Cavity Expansion Models Using Cone Penetrometer Analogs." *Vadose Zone Journal*, 15(3).

- Salgado, R. (1993). Analysis of penetration resistance in sands, University of California, Berkeley.
- Salgado, R., Mitchell, J., and Jamiolkowski, M. (1997). "Cavity expansion and penetration resistance in sand." *Journal of Geotechnical and Geoenvironmental Engineering*, 123(4), 344-354.
- Stewart, J., Crouse, C., Hutchinson, T. C., Lizundia, B., Naeim, F., and Ostadan, F. (2012). "Soil-Structure Interaction for Building Structures | NIST."
- Taboada, A., Chang, K. J., Radjaï, F., and Bouchette, F. (2005). "Rheology, force transmission, and shear instabilities in frictional granular media from biaxial numerical tests using the contact dynamics method." *Journal of Geophysical Research: Solid Earth*, 110(B9).
- Terzaghi, K., Peck, R. B., and Mesri, G. (1996). Soil mechanics in engineering practice, John Wiley & Sons.
- Trueman, E. (1966). "Observations on the burrowing of Arenicola marina (L.)." *Journal of Experimental Biology*, 44(1), 93-118.
- Trueman, E. (1967). "The dynamics of burrowing in Ensis (Bivalvia)." *Proceedings of the Royal Society of London B: Biological Sciences*, 166(1005), 459-476.
- Trueman, E., Brand, A., and Davis, P. (1966a). "The dynamics of burrowing of some common littoral bivalves." *Journal of Experimental Biology*, 44(3), 469-492.
- Vaid, Y., and Sasitharan, S. (1992). "The strength and dilatancy of sand." *Canadian Geotechnical Journal*, 29(3), 522-526.
- Wallace, H. (1968). "The dynamics of nematode movement." *Annual Review of Phytopathology*, 6(1), 91-114.
- White, D. J., and Bolton, M. D. (2005). "Comparing CPT and pile base resistance in sand." *Proceedings of the Institution of Civil Engineers-Geotechnical Engineering*, 158(1), 3-14.
- White, D. J., and Lehane, B. M. (2004). "Friction fatigue on displacement piles in sand." *Geotechnique*, 54(10), 645–658.
- Winter, A. G., Deits, R. L., and Dorsch, D. S. "Critical timescales for burrowing in undersea substrates via localized fluidization, demonstrated by RoboClam: a robot inspired by Atlantic razor clams." *Proc., ASME 2013 International Design Engineering Technical Conferences and Computers and Information in Engineering Conference*, American Society of Mechanical Engineers, V06AT07A007-V006AT007A007.
- Winter, A. G., Deits, R. L. H., Dorsch, D. S., Slocum, A. H., and Hosoi, A. E. (2014). "Razor clam to RoboClam: burrowing drag reduction mechanisms and their robotic adaptation." *Bioinspiration & Biomimetics*, 9(3), 036009.
- Winter, A. G., Deits, R. L. H., and Hosoi, A. E. (2012). "Localized fluidization burrowing mechanics of Ensis directus." *Journal of Experimental Biology*, 215(12), 2072-2080.
- Winter, A. G., Hosoi, A., Slocum, A. H., and Deits, R. L. "The design and testing of RoboClam: A machine used to investigate and optimize razor clam-inspired burrowing mechanisms for engineering applications." *Proc., ASME 2009 International Design Engineering Technical Conferences and Computers and Information in Engineering Conference*, American Society of Mechanical Engineers, 721-726.
- Wu, W., and Ladjal, S. (2014). "Scale effect of cone penetration in sand." *3rd International Symposium on Cone Penetration Testing*, Las Vegas, Nevada, USA, 459-465.
- Yu, H.-S. (2000). Cavity expansion methods in geomechanics, Springer Science & Business Media.
- Yu, H.-S. (2006). "The First James K. Mitchell Lecture In situ soil testing: from mechanics to interpretation†." *Geomechanics and Geoengineering: An International Journal*, 1(3), 165-195.
- Yu, H., and Carter, J. (2002). "Rigorous similarity solutions for cavity expansion in cohesive-frictional soils." *International Journal of Geomechanics*, 2(2), 233-258.
- Yu, H., and Mitchell, J. (1998). "Analysis of cone resistance: review of methods." *Journal of Geotechnical and Geoenvironmental Engineering*, 124(2), 140-149.
- Zhang, Z., and Wang, Y.-H. (2015). "Three-dimensional DEM simulations of monotonic jacking in sand." *Granular Matter*, 17(3), 359-376.
- Zhou, H., Liu, H., Kong, G., and Cao, Z. (2014). "Analytical solution for pressure-controlled elliptical

cavity expansion in elastic–perfectly plastic soil." *Geotechnique letters*, 4(2), 72-78. Zhuang, P.-Z., Yu, H.-S., and Hu, N. (2018). "Size-dependent finite strain analysis of cavity expansion in frictional materials." *International Journal of Solids and Structures*, 150, 282-294.